Research Square

Preprints are preliminary reports that have not undergone peer review.
They should not be considered conclusive, used to inform clinical practice,
or referenced by the media as validated information.

Kinetic description and numerical study of a network of noisy resonate and fire neurons

Nicolas Zadeh

nicolaszadeh@outlook.com

Independent researcher https://orcid.org/0009-0009-7819-8196

Research Article

Keywords: Resonate and fire neuron, Fokker-Planck equation, kinetic partial differential equation, finite difference method, upwind scheme

Posted Date: October 8th, 2026

DOI: https://doi.org/10.21203/rs.3.rs-10781072/v2

License: This work is licensed under a Creative Commons Attribution 4.0 International License.
Read Full License

Additional Declarations: The authors declare no competing interests.

Kinetic description and numerical study of a network of noisy resonate and fire neurons

Nicolas Zadeh*

ARTICLE INFO

Keywords:
Resonate and fire neuron
Fokker-Planck equation
Kinetic partial differential equation
Finite difference method
Neuron network
Structure preserving scheme

MSC: 35Q84; 82C31; 65M06; 92C20

Abstract

Networks of coupled resonate and fire neurons are studied in their mean-field limit through the derivation of a nonlinear kinetic Fokker-Planck equation in a half-plane with a threshold-reset mechanism. A finite-difference scheme adapted to the structure of the equation is introduced and studied, with non-negativity and mass-preservation properties proved rigorously. Numerical experiments then illustrate the structural properties of the scheme, compare it with naive discretizations, and assess the agreement between the mean-field equation and finite-size stochastic particle simulations. The simulations exhibit several dynamical regimes, including reset-driven relaxation, damped subthreshold oscillations, and long-lived population-level oscillations. Long-time simulations further provide numerical evidence for relaxation toward steady profiles, assessed through relative-entropy functionals with respect to computed long-time states.

1. Introduction

Basic components of the nervous system, neurons communicate via the emission of an action potential: as soon as a given firing potential equal to -55 mV is reached, the membrane potential of these electrically charged cells will briefly *spike*, going quickly, on the order of a millisecond, from -55 mV to 40 mV then to -75 mV; finally slowly going back to the resting value of -65 mV. The complex fast/slow dynamics corresponding to this phenomenon were well captured by the pioneering work of Hodgkin and Huxley [39], through a system of nonlinear differential equations describing the ionic mechanisms responsible for these changes. The considerable complexity of this description, associated with its inherently large computational cost, led to a quest for simpler models.

As such, the integrate and fire (IF) model [49] became one of the main centers of attention when it comes to representing the evolution of a neuron's membrane potential, especially for the mathematical community. Indeed, it is easy to understand and models this important spiking feature shared by many neurons, but also, the mean-field approximation corresponding to this model [11, 26, 56] leads to a Fokker-Planck equation which is very rich when it comes to its mathematical properties [15, 16, 21, 28, 40].

However, even though an important attribute of some areas of the brain is the ability to take into account the complex structures in frequency of incoming signals, as can be seen for example with the resonant behavior of the multi-functional stellate cells in the entorhinal cortex [3, 31, 60], the IF neuron poorly selects inputs based on the frequency content. Indeed, as its name suggests, in this model a neuron essentially *integrates* inputs, tending to favor, at fixed excitatory input amplitude, higher frequencies of arrival.

Moreover, the IF model cannot display subthreshold membrane oscillations, although such a phenomenon can occur in the Hodgkin-Huxley model for suitable parameter values and is observed in various types of neurons [36, 50, 64].

These limitations motivate the use of another class of reduced neuronal models, usually called resonators.

Multiple popular single-neuron models, such as the Morris-Lecar [52] (for some parameter values), the FitzHugh-Nagumo [33], or the Hodgkin-Huxley model [39], are resonators, the first two leading to mean-field partial differential equations (PDE) descriptions [37, 51] following the kinetic formalism.

Since the aforementioned resonator models have an important computational cost, another model [45] has been built, which while still being simple, and computationally cheap (see Table 1 below), allows one to complement the IF one: the resonate and fire (RF) model, whose properties have been studied for many years now [6, 8, 9, 19, 31, 53, 55, 65, 66]. This computational simplicity is not only useful for biological modeling: it also explains the recent renewed

*Corresponding author
nicolaszadeh@outlook.com (N. Zadeh)
ORCID(s): 0009-0009-7819-8196 (N. Zadeh)

Table 1
Approximate computational cost of the presented single-neuron models, data from [44]. Here FLOPS denotes the number of floating point operations needed by the model during a 1 ms simulation.

Model	FLOPS
Integrate and fire	5
Resonate and fire	10
FitzHugh-Nagumo	72
Morris-Lecar	600
Hodgkin-Huxley	1200

interest in RF-type units in the spiking neural network and neuromorphic computing literature, where their oscillatory dynamics can be used to extract frequency information from temporal signals [71].

Interestingly, as for the integrate and fire model, the RF model admits a simple electrical interpretation: it can be viewed as an RLC parallel circuit [31, 65], consistently with the linearization of the Hodgkin-Huxley model used to obtain resonator-like properties [50, 67].

To describe the dynamics of a network of such neurons under external stimulation, it is natural to seek a mean-field formulation. Mean-field partial differential equations provide a natural framework for the description of large neuronal populations, and have been developed in several directions, including nonlinear noisy integrate-and-fire models, elapsed-time equations, stochastic neural fields, and kinetic voltage-conductance models; see, for instance, [17] for a recent review. In the RF setting, such a formulation is expected to provide a tractable description of the qualitative behavior of the neuronal assembly, while still retaining, at least formally, the relative simplicity of the underlying single-neuron model.

In this work, we study, for the first time to our knowledge, a mean-field equation characterizing the electrical activity of a population of RF neurons. In its simplest form, assuming that the neurons of the population have electrical characteristics described by constants ω_0, τ, that the spike train external to the population has rate ν_{ext} and that $b \in \mathbb{R}$, $a_0 > 0, a_1 > 0$ are determined by the connectivity parameters of the network, we formally derive the following nonlinear kinetic Fokker-Planck equation, where $f(x, v, t)$ denotes the probability density of neurons with voltage $x < u_{\text{F}}$ and voltage velocity $v = \dot{x}$ at time $t \in [0, T)$, with $T > 0$:

$$\begin{aligned}\partial_t f(x,v,t) + v\partial_x f(x,v,t) + \partial_v \left[\left(-\frac{v}{\tau} - x\omega_0^2 + b(\nu_{\text{ext}} + N(t))\right) f(x,v,t)\right] \\ - (a_0 + a_1 N(t))\partial_v^2 f(x,v,t) = N(t)\delta_{(u_{\text{R}},0)}(x,v),\end{aligned} \tag{1}$$

the expression of the activity N of the network, understood as the mean number of spikes per unit time, being given by:

$$N(t) = \int_{v>0} v\, f(u_{\text{F}}, v, t)\, \mathrm{d}v. \tag{2}$$

In works like [13], numerical simulations of solutions to mean-field PDEs allowed to assess the agreement between the mean-field approximation and the behavior of large networks of identical neurons. However, the application of classical discretizations to equation (1) led to non-physical results in highly nonlinear regimes, as illustrated in Tables 3 and 4. A scheme adapted to the specificities of the equation was therefore needed.

Yet the theoretical study of this equation is technical. Indeed, the phase space is unbounded in both directions without being the whole space, so that the relevant kinetic trace theory is already non-standard; see [34, 35] for related difficulties in a neighbouring model. In addition, the differential operator at play is both nonlinear and degenerate, while the reset mechanism gives rise to a singular right-hand side. These features constitute significant hurdles already at the level of a basic well-posedness theory, before one could even consider finer properties of the corresponding solutions.

Accordingly, assuming a well-behaved initial datum, we focus on the two fundamental physical properties expected from a solution: preservation of non-negativity, through

Property 1 (Non-negativity)**.**

$$\forall t \in [0, T), \qquad f(\cdot,\cdot,t) \geq 0 \quad \text{and} \quad N(t) \geq 0,$$

and conservation of mass, as in

Property 2 (Conservation of mass)**.**

$$\forall t \in [0,T), \qquad \int_{x<u_F} \int_{v\in\mathbb{R}} f(x,v,t)\,\mathrm{d}v\,\mathrm{d}x = 1.$$

We then introduce an original semi-implicit Euler upwind-type finite difference scheme with adapted numerical boundary conditions. Under suitable dynamical conditions, this scheme satisfies the numerical counterparts of Properties 1 and 2, respectively Properties 3 and 4, which are proved rigorously. The expected agreement between the mean-field limit and the point neuron networks, where the latter are simulated using the neuron/synapse simulator Brian 2 [62] is observed in Section 4.2, supporting the relevance of the adopted mean-field formalism.

From the standpoint of pure numerical analysis, the expected properties 3 and 4 are confirmed numerically in Tables 3 and 4. The same experiments indicate a convergence order of 1 in (x, v, t).

The scheme then allows us to highlight four representative dynamical regimes: reset-driven, subthreshold damped oscillatory, far-from-threshold, and strongly oscillatory. On longer time intervals, these experiments suggest relaxation toward numerical steady states for the parameters considered. This motivates the introduction of a relative entropy-type functional with respect to the computed long-time profiles, and points to open questions concerning steady states and entropy decay.

It should be noted that the present model, which we call *Network of Noisy Resonate and Fire neurons* (NNRF) is intended as a complement to existing models for neuronal networks, rather than as a redundant reformulation of them. Indeed, compared with:

- the NNLIF model, the voltage-velocity phase space makes the timing of threshold crossings depend not only on the membrane potential, but also on the velocity distribution;
- voltage-conductance models [13, 14, 27, 34, 35, 54], the threshold mechanisms are different. In an inhibitory voltage-conductance regime, the voltage drift may point away from the firing threshold, so that the deterministic transport does not carry mass toward firing at first. In the NNRF model, by contrast, the relation $\dot{x} = v$ implies that mass with positive velocity will move towards the threshold. Thus the NNRF model can exhibit firing in phase-space configurations for which a conductance-driven voltage model would remain subthreshold;
- FitzHugh-Nagumo-type mean-field equations [33, 51], these equations also describe resonator dynamics, but they do not contain the same firing-boundary and reset-source mechanism; moreover their phase-space geometry is organized by more complex nullclines.

The NNRF equation therefore provides an intermediate kinetic model: simpler and more geometrically transparent than fast-slow conductance- or FitzHugh-Nagumo-based descriptions, but richer than the NNLIF model from the point of view of phase-space transport.

Preliminary results of this work were presented at the 13th European Conference on Mathematical and Theoretical Biology (ECMTB 2024) in Toledo, Spain.

All numerical experiments presented in this work are fully reproducible. The complete solver implementation and the scripts used to generate the figures are publicly available on GitHub. An archived version of the code associated with this article is provided via Zenodo [69].

The outline of the rest of this paper is as follows. In Section 2, we establish the formal mean-field limit description, starting with the RLC circuit analogy, with some heuristics presenting the expected behavior of the model and explaining the chosen boundary conditions; we also distinguish it from other PDE models present in the literature. Then, in Section 3, we present the semi-implicit upwind finite difference scheme adapted to this framework and prove preservation of non-negativity and conservation of mass under suitable Courant-Friedrichs-Lewy (CFL) and computational domain largeness conditions. In Section 4, the results of some numerical simulations are displayed, supporting the validity of the mean-field model by illustrating some already known behaviors of this type of neurons, as well as comparing it with simulations performed with a large number of interconnected neurons obeying the RF model equation. The structural properties of our method will also be illustrated numerically. Different representative regimes are displayed, and observations related to long time behavior are made. The paper ends with some concluding remarks in Section 5.

The appendices are organized as follows:

A. The derivation of the Fokker-Planck equation (1).

B. The proof of a discrete integration-by-parts lemma, used in the proof of mass conservation.

C. A precise description of the standard schemes used for comparison in Section 4.1.

D. The parameter values used in the experiments on representative regimes.

This manuscript is a short version of a preprint available on Cambridge Open Engage [70], which contains more detailed computations, formulae for all the discrete functionals used in the paper, as well as additional figures and remarks.

2. The resonate and fire model

2.1. The single neuron model

Setting the resting potential V_0 equal to 0, the parallel circuit from the single neuron study of [65, Figure 1.a)] takes the form shown in Figure 1.

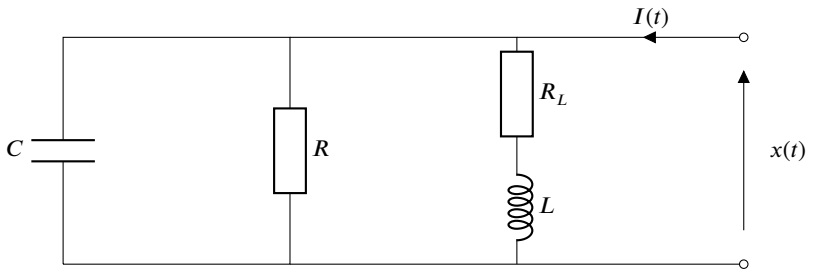


Figure 1: Chosen description of a RF neuron in our work

In a simplification effort, as in [31], we do not introduce a time-dependent conductance $g(t)$ which would allow us to take into account cell-intrinsic noise (see [68] for a review on the subject and [30, 65] for experimental results obtained with the time-dependent conductance). From now on I denotes the input current external to the neuron under study.

Let x denote the voltage across the capacitor. The basic laws of electricity give, with

$$\omega_0 := \sqrt{\frac{R+R_L}{RLC}}, \qquad \tau := \frac{RLC}{L+R_L RC},$$

the following linear equation:

$$\ddot{x} + \frac{1}{\tau}\dot{x} + \omega_0^2 x = \frac{R_L}{LC} I + \frac{1}{C}\frac{\mathrm{d}I}{\mathrm{d}t}, \tag{3}$$

which, by introducing a velocity variable $v := \dot{x}$, can be rewritten as the following system, for $x < u_{\mathrm{F}}$:

$$\begin{cases} \dot{x} = v \\ \dot{v} = -\frac{1}{\tau} v - \omega_0^2 x + \frac{R_L}{LC} I + \frac{1}{C}\frac{\mathrm{d}I}{\mathrm{d}t}. \end{cases} \tag{4}$$

To complete our description, we explain the chosen simplification to represent the spiking mechanism, which gives rise to the nonlinearity: for any positive v, whenever the potential x reaches a given value u_{F} called the threshold value (which is the actual membrane potential threshold value minus the actual resting potential), the neuron is said to spike, and is immediately sent to a reset point. We choose here to define the voltage at reset equal to some fixed $u_{\mathrm{R}} < u_{\mathrm{F}}$, taking the velocity v_{R} at reset equal to 0 as in [9, 2.1.2], motivated by the potential function reaching a local minimum with respect to time at the moment of hyperpolarization.

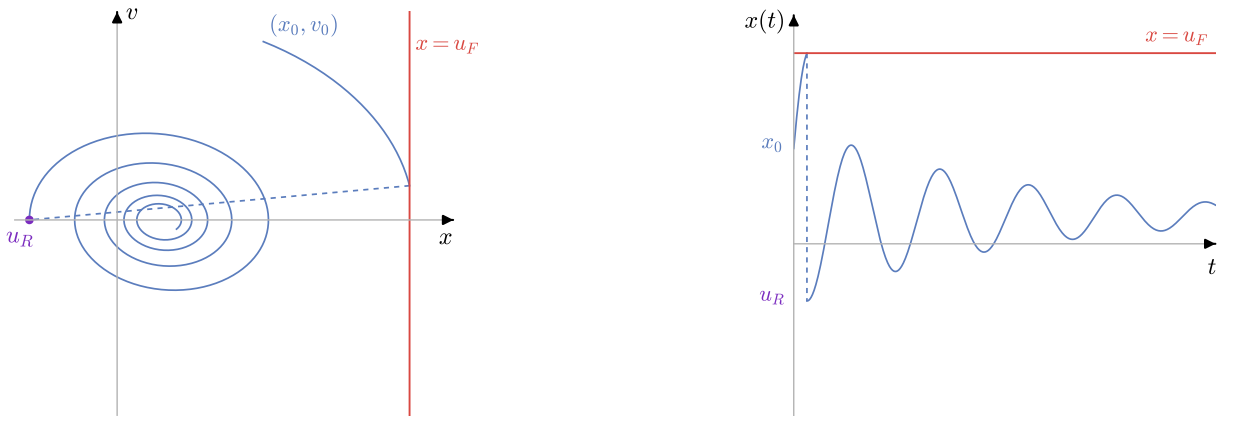


Figure 2: Example of single-neuron RF dynamics governed by $\ddot{x} + \tau^{-1}\dot{x} + \omega_0^2 x = S_0$ with reset and subthreshold oscillations over $T = 12\,\mathrm{s}$. Parameters: $u_\mathrm{F} = 1\,\mathrm{mV}$, $u_\mathrm{R} = -0.3\,\mathrm{mV}$, $x_0 = 0.5\,\mathrm{mV}$, $v_0 = 2.1\,\mathrm{mV\,s^{-1}}$, $S_0 = 71/75\,\mathrm{mV\,s^{-2}}$ $\omega_0 = 2.5\,\mathrm{rad\,s^{-1}}$, and $\tau = 3\,\mathrm{s}$.

Figure 2 illustrates the resulting dynamics for a single neuron: the trajectory can display subthreshold damped oscillations before reaching the threshold and being reset.

The next simulation shown in Figure 3, obtained with the reference tool Brian 2 [62], allows us to show that our single neuron model can reproduce the range of behaviors Izhikevich describes in his seminal article [45]. We observe subthreshold damped oscillations, as well as spiking induced by inhibitory inputs. This illustrates a key difference with the integrate-and-fire model, for which spiking can only be generated by direct integration of excitatory input. It should be noted that precisely to focus on phenomena of this type, we will assume $4\tau^2\omega_0^2 > 1$ throughout the paper.

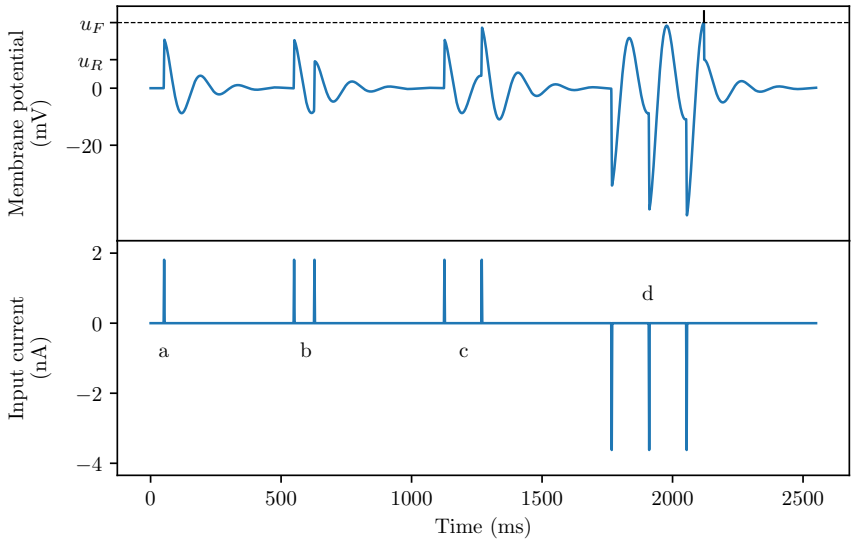


Figure 3: Single RF neuron response to a train of inputs. a) Isolated pulse of weak amplitude: the circuit does not receive enough energy to reach the threshold and displays subthreshold damped oscillations. b) Doublet with unfavorable timing: the amplitude of the response decreases. c) Doublet with favorable timing: the amplitude of the response increases. d) Favorable timing combined with a larger input amplitude produces spiking, *even in an inhibitory setting*. Parameters, from [65, Figure 3]: $u_\mathrm{F} = 23\,\mathrm{mV}$, $u_\mathrm{R} = 10\,\mathrm{mV}$, $u_\mathrm{L} = 0\,\mathrm{mV}$, $R = 500\,\mathrm{M\Omega}$, $R_L = 25\,\mathrm{M\Omega}$, $C = 0.21\,\mathrm{nF}$, $L = 2.5\,\mathrm{MH}$. Stimulus amplitudes: 1.81 nA for a), b), and c), and 3.62 nA for d). Inter-stimulus intervals: 76 ms for b), 141 ms for c), and 141.5 ms for d).

Remark 2.1. In these models, in general, the *phenomenological* electrical constants can be non-positive. However, we will assume them to be positive throughout this work, in agreement with the measures in the literature for neurons of the entorhinal cortex (see [31, Table 2]).

2.2. The population model and the Fokker-Planck equation

Let us now consider a sparsely connected network of n identical RF neurons. We assume that n is large enough for a mean-field description to be relevant, while the population remains homogeneous enough for the same sparse connectivity structure to be used throughout the network. In particular, as in the sparse-network approximation of [11], correlations between the fluctuating parts of the synaptic inputs of different neurons are neglected, apart from those induced by the common population activity. We assume that the evolutions of all these neurons obey equation (4), with fixed parameters R, R_L, L and C.

The goal of this section is to obtain a Fokker-Planck type equation for the probability density function f depending on the variables x, v, t which will describe the group behavior of this network.

Receiving c_{int} randomly chosen connections from other neurons in the network, as well as c_{ext} connections from neurons outside of the network, each neuron i is described by the vector $\begin{pmatrix} x_i \\ v_i \end{pmatrix}$, x_i being its membrane potential and v_i its voltage-velocity variable, satisfying $\dot{x}_i = v_i$ almost everywhere between reset events.

In the literature, what is then usually considered as an input for a given neuron of the population, is an incoming postsynaptic current of the following form, δ being the Dirac delta at 0:

$$I(t) = J_{\text{E}} \sum_{i=1}^{c_{\text{E}}} \sum_{j \in \mathbb{N}} \delta(t - t^i_{\text{E}_j}) - J_{\text{I}} \sum_{i=1}^{c_{\text{I}}} \sum_{j \in \mathbb{N}} \delta(t - t^i_{\text{I}_j}), \tag{5}$$

with $J_{\text{E}} \geq 0$ the strength of excitatory synapses, $J_{\text{I}} \geq 0$ the strength of inhibitory ones; c_{E} the number of excitatory presynaptic neurons connections, c_{I} the number of inhibitory ones (thus giving us $c_{\text{int}} + c_{\text{ext}} = c_{\text{E}} + c_{\text{I}}$); $t^i_{\text{E}_j}$ (respectively $t^i_{\text{I}_j}$) the time of the j^{th} spike coming from excitatory (respectively inhibitory) neurons of the network, coming from the i^{th} presynaptic neuron.

However this form of postsynaptic current would raise issues in our model, since a derivative of the input current needs to be computed in (4), which would lead to a derivative of a white noise, and hence to a much more complicated mathematical setting. This problem was not encountered yet in the single neuron case as the input current was chosen to be constant in [30] (the source of noise coming from stochastic conductance), time-dependent but fixed in [31], or as in [53, 65], a noisy source term was considered, but without being explicitly related to the external current.

We circumvent this difficulty by considering a well-known, more realistic form of postsynaptic current. Assuming that the presynaptic spike train is of the form:

$$I^{\text{pre}}(t) = J_{\text{E}} \sum_{i=1}^{c_{\text{E}}} \sum_{j \in \mathbb{N}} \delta(t - t^i_{\text{E}_j}) - J_{\text{I}} \sum_{i=1}^{c_{\text{I}}} \sum_{j \in \mathbb{N}} \delta(t - t^i_{\text{I}_j}), \tag{6}$$

we suppose, as in [56][15.2.5], that the aforementioned fixed neuron in our population receives a post-synaptic current I following the equation:

$$\tau_{\text{syn}} \frac{\mathrm{d}I}{\mathrm{d}t} = -I(t) + I^{\text{pre}}(t), \tag{7}$$

in a distributional sense.

We now assume that the spiking times of the excitatory and inhibitory neurons, displayed in equation (6), follow independent Poisson processes with instantaneous rate $\nu(t)$, the independence assumption being supported by the sparsity of the network. This rate ν corresponding to the spiking both inside and outside of the network, we can write $\nu(t) = N(t) + \nu_{\text{ext}}$, with N defined as the activity of our population (as in the number of spikes per second), and ν_{ext} the activity of the neurons connected to our population, which we will assume to be a given constant. We also assume the absence of a synaptic delay to simplify the model at first. [1]

[1] Including delays would be natural from both the mathematical and modeling points of view, as in the integrate-and-fire and FitzHugh-Nagumo settings [5, 12, 20, 22–24, 43, 48].

We would now like to take advantage of the classical idea going back to [57], and later used in [11, 13] for example, by using the diffusion approximation on the right-hand side of (3), which we will denote:

$$S := \frac{R_L}{LC} I + \frac{1}{C} \frac{\mathrm{d}I}{\mathrm{d}t}. \tag{8}$$

In this approximation (here suitable, as in [56], provided the size of the kicks is small enough, i.e. $\frac{J_\mathrm{E}}{C\tau_\mathrm{syn}}, \frac{J_\mathrm{I}}{C\tau_\mathrm{syn}}$ small enough), the equation (4) gives birth to a Fokker-Planck equation under a simplifying two-dimensional closure, as detailed in Appendix A.

Let us define the domains

$$\Omega := (-\infty, u_\mathrm{F}) \quad \text{and} \quad E := \Omega \times \mathbb{R}. \tag{9}$$

For $(x, v) \in E$, and $t > 0$, we denote by $f(x, v, t)$ the probability density function associated with the pair (X_t, V_t), where X_t and V_t represent respectively the membrane potential and the associated velocity of a typical neuron representative of the network at time t.

Given an initial probability density function f^0 defined on E, the evolution of f below the voltage threshold is then formally described by the following Fokker-Planck equation, for $t > 0$:

$$\begin{aligned} \partial_t f(x,v,t) + v\partial_x f(x,v,t) + \frac{\partial}{\partial v}\left[\left(-\frac{v}{\tau} - x\omega_0^2 + b^\mathrm{ext}\nu_\mathrm{ext} + b^\mathrm{int}N(t)\right) f(x,v,t)\right] \\ - \left(a_0 + a_1 N(t)\right)\partial_v^2 f(x,v,t) = 0, \end{aligned} \tag{10}$$

where

$$\begin{cases} b^\mathrm{ext} := \frac{c_\mathrm{E}^\mathrm{ext} J_\mathrm{E}^\mathrm{ext} - c_\mathrm{I}^\mathrm{ext} J_\mathrm{I}^\mathrm{ext}}{C\tau_\mathrm{syn}} \\ b^\mathrm{int} := \frac{c_\mathrm{E}^\mathrm{int} J_\mathrm{E}^\mathrm{int} - c_\mathrm{I}^\mathrm{int} J_\mathrm{I}^\mathrm{int}}{C\tau_\mathrm{syn}} \end{cases} \qquad \begin{cases} a_0 := \frac{c_\mathrm{E}^\mathrm{ext} J_\mathrm{E}^{\mathrm{ext}\,2} + c_\mathrm{I}^\mathrm{ext} J_\mathrm{I}^{\mathrm{ext}\,2}}{2C^2\tau_\mathrm{syn}^2}\nu_\mathrm{ext} \\ a_1 := \frac{c_\mathrm{E}^\mathrm{int} J_\mathrm{E}^{\mathrm{int}\,2} + c_\mathrm{I}^\mathrm{int} J_\mathrm{I}^{\mathrm{int}\,2}}{2C^2\tau_\mathrm{syn}^2}. \end{cases} \tag{11}$$

Since we assume that there is no neuron with a membrane potential above u_F, we impose a 0 incoming trace at the firing boundary. Because of the characteristics of the transport operator associated with equation (10), that corresponds to $f(u_\mathrm{F}, v, t)$ vanishing for all non-positive values of v (a *no-inflow* condition).

Arbitrarily negative membrane potentials not being physically relevant, we also impose the decay condition

$$\forall v \in \mathbb{R}, \qquad f(-\infty, v, t) = 0. \tag{12}$$

Let us now introduce the fluxes in the x and v directions, denoted respectively by F_x and F_v:

$$\begin{cases} F_x(x,v,t) := v f(x,v,t) \\ F_v(x,v,t) := \left(-\frac{v}{\tau} - x\omega_0^2 + b^\mathrm{ext}\nu_\mathrm{ext} + b^\mathrm{int}N(t)\right) f(x,v,t). \end{cases} \tag{13}$$

Setting

$$a(t) := a_0 + a_1\, N(t), \tag{14}$$

so as not to have mass leakage at infinite velocities, we impose another boundary condition, this time zero-flux in the velocity direction:

$$\forall x \in \Omega, \qquad F_v(x, \pm\infty, t) - a(t)\partial_v f(x, \pm\infty, t) = 0. \tag{15}$$

Because of the definition of F_x, denoting by $N(t)$ the activity of the network, i.e. the mean number of spikes per unit time, one gets, by formal Green identity, the integral formula (2) for $t > 0$. We also define an initial activity by means of the equation:

$$N^0 := \int_{v>0} v\, f^0(u_\mathrm{F}, v)\, \mathrm{d}v. \tag{16}$$

Let us finally complete our description by the reset mechanism. As it is the case in the integrate and fire model, the reset will appear in the form of a mass displacement phenomenon: since we neglect any delay or refractory period, as soon as a neuron gets to the threshold value of its voltage variable from below, it invokes a spike and gets immediately reset at the point $(u_R, 0)$, ready to participate to the group dynamics again.

We thus get, for $x < u_F$, $v \in \mathbb{R}$:

$$\partial_t f(x,v,t) + \partial_x F_x(x,v,t) + \partial_v F_v(x,v,t) - a(t)\partial_v^2 f(x,v,t) = N(t)\delta_{(u_R,0)}(x,v). \tag{17}$$

When one assumes $b^{\text{int}} = b^{\text{ext}}$, the simplified form (1) seen in the introduction appears.

With the constraint that $f(\cdot,\cdot,t)$ remains a probability density function for all times under consideration, the preceding discussion can be summarized by the following formal description of our population on a time interval $[0,T)$, where T is some time in $(0,+\infty]$, on which the description is assumed valid:

$$\begin{cases} \partial_t f(x,v,t) + \partial_x F_x(x,v,t) + \partial_v F_v(x,v,t) - a(t)\partial_v^2 f(x,v,t) = N(t)\delta_{(u_R,0)}(x,v), \\ N(t) = \displaystyle\int_{v>0} v\, f(u_F,v,t)\,\mathrm{d}v, \\ \forall v < 0, \qquad f(u_F,v,t) = 0, \qquad\qquad \forall v \in \mathbb{R}, \qquad f(-\infty,v,t) = 0, \\ \forall x < u_F, \qquad F_v(x,\pm\infty,t) - a(t)\,\partial_v f(x,\pm\infty,t) = 0, \\ f^0 \geq 0, \qquad \displaystyle\int_E f^0 = 1, \qquad N^0 = \int_{v>0} v\, f^0(u_F,v)\,\mathrm{d}v. \end{cases} \tag{18}$$

Further references to the NNRF model will correspond to system (18).

Remark 2.2. One should keep in mind that this model is limited in the sense that the electric constants corresponding to different neurons in the EC layer II for example can differ from one another, which may thus forbid this mean-field formalism if one wants to model a population of heterogeneous neurons, even in a localized region of the brain as the one we just described.

Remark 2.3. As was the case in the original works on the NNLIF model, the derivation of the Fokker-Planck equation associated with Problem (18) followed in this subsection and in Appendix A is formal. A fully rigorous derivation from the underlying interacting particle system would require proving a suitable mean-field limit, or propagation of chaos result. In addition, the PDE formulation used here represents the population activity by a time function $N(t)$. At the level of the particle system, however, the natural object is the cumulative spike-counting process, and in the limit one must justify that this cumulative activity is absolutely continuous in time so that its time derivative can be identified with the boundary flux appearing in the Fokker-Planck formulation. Such results are not trivial, and the associated proofs were already technical in the case of the NNLIF model [25, 26].

2.3. General heuristics for the NNRF model

From now on, for simplicity we take

$$b^{\text{ext}} = b^{\text{int}} = b.$$

As is customary in the physics literature for the Fokker-Planck equation, we denote by μ the drift associated with (17), that is, for all $(x,v) \in E$ and $t > 0$,

$$\mu(x,v,t) := \begin{pmatrix} v \\ -\dfrac{v}{\tau} - x\omega_0^2 + b\left(\nu_{\text{ext}} + N(t)\right) \end{pmatrix}. \tag{19}$$

We write

$$\mu_1(x,v,t) := v \qquad \mu_2(x,v,t) := -\frac{v}{\tau} - x\omega_0^2 + b\left(\nu_{\text{ext}} + N(t)\right)$$

for its two components.

The solution to Problem (18) results from the interplay between the transport generated by μ, the diffusion acting in the velocity variable, and the redistribution of mass produced by the reset source [59].

For fixed $N(t)$, the drift vanishes at the point

$$P(t) := \left(\frac{b\left(\nu_{\text{ext}} + N(t)\right)}{\omega_0^2}, 0 \right). \tag{20}$$

The transport therefore induces a damped spiral-like motion around the instantaneous center $P(t)$, as illustrated in Figure 4. This already suggests that the relative positions of the initial density, the reset point $(u_{\text{R}}, 0)$ and the center $P(t)$ play an essential role in the dynamics.

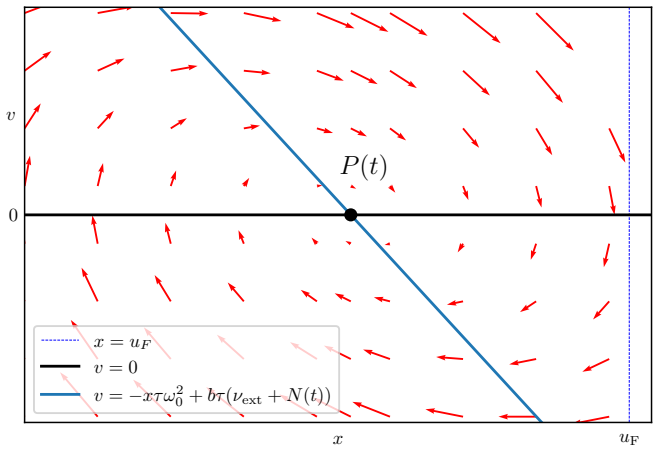


Figure 4: Vector field μ on the (x, v) grid, at fixed activity $N(t) = 0$. Parameters: $u_{\text{F}} = 9$, $b = 1$, $\nu_{\text{ext}} = 1$, $\omega_0 = 2$, and $\tau = 2$.

A second important feature is that the diffusion acts only in the velocity variable. At first sight, one might therefore expect the density to spread only in the v direction. However, the transport term $v\partial_x$ couples the two variables and, formally, Hörmander's sums of squares condition [42] is satisfied in the interior. Consequently, one expects a hypoelliptic regularization mechanism: even though the second-order operator acts only in v, the density spreads in both v and x for positive times.

This observation is relevant for the understanding of the reset mechanism, since it indicates that boundary activity is not produced only by deterministic transport toward the threshold: velocity diffusion, combined with the kinetic coupling, may also contribute to the creation of outgoing flux. The activity $N(t)$ is therefore not merely an observable of the dynamics, but also a feedback variable. It shifts the center $P(t)$ and changes the diffusion coefficient through (14), thereby coupling firing, transport, and noise intensity. This feedback leaves open the possibility of regimes in which the activity becomes very large.

These observations also explain why the natural continuous phase space is the half-plane $x < u_{\text{F}}$, rather than a bounded voltage interval crossed with $\mathbb{R}_v$. Since $N(t)$ is generated by the outgoing flux at the firing boundary and is then reinjected through the reset source, there is no obvious a priori upper bound on the activity. Consequently, the center $P(t)$ may undergo large displacements. If $b < 0$, large activity shifts $P(t)$ toward negative voltages. If $b > 0$, a center located far to the right can generate large spiraling excursions toward negative voltages, especially for mass lying initially or after reset in the region $v < 0$. In either case, imposing an artificial finite lower bound on x would not be naturally compatible with the possible transport geometry of the model. This motivates the choice of the unbounded phase space $x < u_{\text{F}}$ and the corresponding boundary condition at $x = -\infty$.

The numerical scheme introduced in the next section is designed to retain, after truncation, the main structural features suggested by these heuristics: kinetic transport in (x, v), degenerate diffusion in v, and reset-driven feedback through $N(t)$.

3. Presentation and properties of the numerical scheme

Armed with this now stronger heuristic understanding of our model and of the a priori behavior of expected solutions, we now start a numerical study of Problem (18).

In the reference article [40], a fine asymptotic property of solutions to a PDE arising in neuroscience which had been proved theoretically beforehand was observed through an astute scheme, which respected the associated structure. More generally, the construction of structure-preserving schemes for Fokker-Planck equations is a classical issue. The Chang-Cooper method [18] is a fundamental example, designed to preserve basic properties such as non-negativity for a one-dimensional drift-diffusion Fokker-Planck equation. In the kinetic setting, other structural questions arise, such as the construction of discretizations for which discrete analogues of the continuous coercive or hypocoercive estimates remain valid [29]; in general, preservation of structure for Fokker-Planck equations remains an active field of research [7].

Because of the complexity of the mechanisms involved in (17), we focus here on two fundamental structural properties of the scheme: preservation of non-negativity and conservation of mass, putting us in a different framework compared to these works we just referenced. In this section, we therefore focus on proving these properties for an original numerical scheme, adapted to our equation.

The three levels of description used in the numerical parts of the paper are summarized in Table 2.

Table 2
Hierarchy of the continuous and discrete problems used in the numerical analysis.

Problem	Mathematical setting	Role in the analysis
Formal NNRF model	Unbounded half-plane with singular reset source	Reference continuous model
Truncated regularized problem	Bounded domain with regularized reset distribution	Continuous problem to be discretized
Finite-difference scheme	Finite grid with adapted boundary conditions	Fully discrete structure-preserving approximation

3.1. Simplification of the continuous problem

We choose to simplify problem (18) in a way which makes it accessible to numerical resolution without losing behavioral richness.

We first replace the Dirac delta with $\rho(x, v)$: a Maxwellian very concentrated around $(u_R, 0)$, truncated to be compactly supported in the half-plane $x < u_F$ and normalized to be of mass 1. We then introduce the open bounded domain $E_{cut} := (x_{min}, u_F) \times (-V, V)$, with $V > 0$ large, $x_{min} < 0$ of large absolute value chosen so that E_{cut} contains the support of ρ. The geometry of this domain is illustrated in Figure 5.

With x_{min} and u_F fixed, the vector field μ has the property of being vertically confining for large enough values of V: at the artificial boundaries $v = \pm V$, its vertical component points inward as soon as V dominates the remaining drift terms. This observation is central in the choice of the truncated velocity domain as it will considerably simplify the boundary conditions. It is also reminiscent of confinement mechanisms studied for nonlinear Fokker-Planck equations, for instance through strong confining potentials in [2]; in our setting the confinement comes directly from the kinetic drift. We therefore make the assumption that V is large enough during the duration of the study of the problem so that μ remains vertically confining. More precisely:

Assumption 1.

$$\forall t \in [0, T), \qquad \mu_2(x, V, t) < 0 \quad \text{and} \quad \mu_2(x, -V, t) > 0.$$

Under this assumption flux can leave the truncated domain only through the lateral boundaries in x.

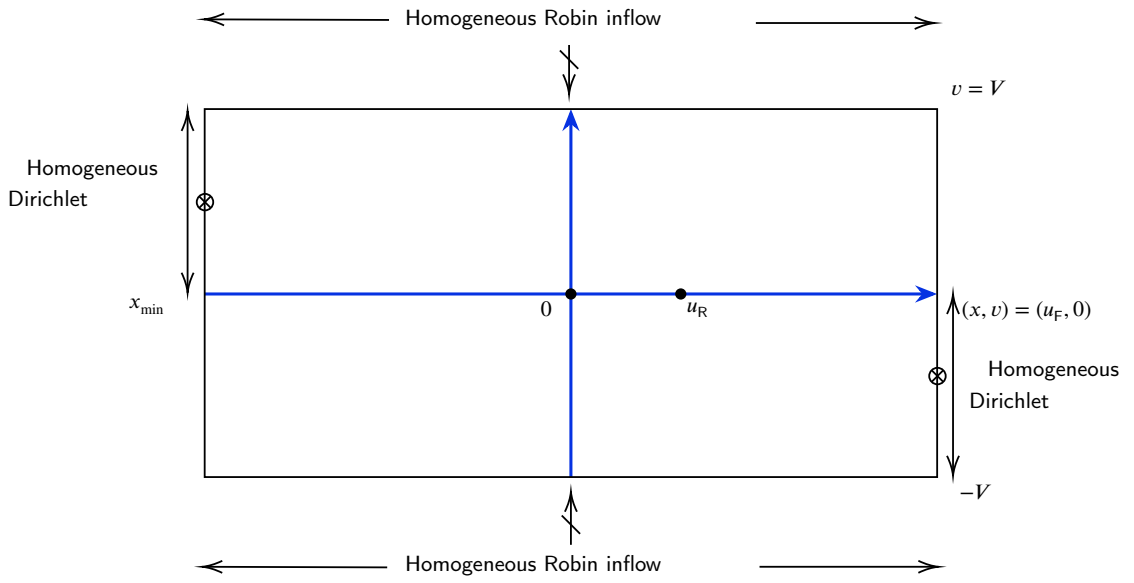


Figure 5: Truncated domain E_{cut} with boundary conditions

We shall now study the following continuous problem, which is the immediate transposition of Problem (18) to E_{cut}:

Equation:

$$\forall (x,v,t) \in E_{\text{cut}} \times (0,T),$$

$$\partial_t f(x,v,t) + v\,\partial_x f(x,v,t) + \frac{\partial}{\partial v}\left(\left[-\frac{v}{\tau} - x\omega_0^2 + b(v_{\text{ext}} + N(t))\right] f(x,v,t)\right) - (a_0 + a_1 N(t))\partial_v^2 f(x,v,t) = N(t)\rho(x,v), \tag{21a}$$

Activity:

$$\forall t \in (0,T), \quad N(t) = \int_{v\in(0,V)} v f(u_F,v,t)\,\mathrm{d}v - \int_{v\in(-V,0)} v f(x_{\min},v,t)\,\mathrm{d}v, \tag{21b}$$

Boundary conditions:

Homogeneous Dirichlet inflow:

$$\forall v \in (0,V), \quad f(x_{\min},v,t) = 0, \tag{21c}$$

$$\forall v \in (-V,0), \quad f(u_F,v,t) = 0, \tag{21d}$$

Homogeneous Robin inflow:

$$\forall x \in (x_{\min},u_F), \quad \mu_2 f(x,\pm V,t) - a(t)\,\partial_v f(x,\pm V,t) = 0, \tag{21e}$$

Physical properties:

$$\forall t \in (0,T), \quad f(\cdot,\cdot,t) \geq 0, \quad \int_{E_{\text{cut}}} f(\cdot,\cdot,t) = 1, \tag{21f}$$

Initial condition:

$$\forall (x,v) \in E_{\text{cut}}, \quad f^0(x,v) \geq 0, \quad \int_{E_{\text{cut}}} f^0 = 1, \tag{21g}$$

$$N^0 = \int_{v\in(0,V)} v f^0(u_F,v)\,\mathrm{d}v - \int_{v\in(-V,0)} v f^0(x_{\min},v)\,\mathrm{d}v. \tag{21h}$$

Remark 3.1. The disjunction of the boundary in an inflow and an outflow part comes naturally from the partially hyperbolic nature of the equation: one shouldn't impose conditions where the dynamics of the flow already give us the information thanks to the exact description of the flow as well as the interior values of our function.

Remark 3.2. The no-inflow boundary conditions (21c) and (21d) prevent artificial mass from entering the truncated domain through the lateral boundaries. Mass is therefore allowed to leave only through the lateral outflow parts, namely $x = u_{\mathrm{F}}$ for $v > 0$ and $x = x_{\min}$ for $v < 0$. The role of Assumption 1 is to ensure that the artificial velocity boundaries $v = \pm V$ are not outflow boundaries for the drift: the vertical component of the drift points inward there. Together with the Robin boundary condition (21e), this prevents loss of mass through $v = \pm V$. The only mass loss to compensate is the lateral outgoing flux, which is exactly measured by $N(t)$ as seen in equation (21b), and reinjected near the reset point through the source term $N(t)\rho$.

3.2. Discrete operators

As explained above, hypoellipticity in the regularized truncated setting suggests interior regularization of solutions to Problem (21) under suitable assumptions on the coefficients and regularized source, provided such solutions exist. Since the phase space is rectangular, the use of a finite difference method seems natural. Such methods are also classical for kinetic Fokker-Planck operators; see for instance [29]. We now introduce the discrete sets and operators used in the scheme.

Definition 1. Let us discretize the intervals $[x_{\min}, u_{\mathrm{F}}]$, $[-V, V]$, and $[0, T]$ uniformly, with constant steps Δx, Δv and Δt; denoting:

- $\mathcal{I} := [\![1, i_{\mathrm{F}} - 1]\!], \quad \overline{\mathcal{I}} := [\![0, i_{\mathrm{F}}]\!],$
- $\forall i \in \overline{\mathcal{I}}, \quad x_i := x_{\min} + i\Delta x$
- $\mathcal{J} := [\![1 - j_{\max}, j_{\max} - 1]\!], \quad \overline{\mathcal{J}} := [\![-j_{\max}, j_{\max}]\!],$
- $\forall j \in \overline{\mathcal{J}}, \quad v_j := j\Delta v,$
- $\mathcal{J}_{\geq 0} := \mathcal{J} \cap \mathbb{N}, \quad \mathcal{J}_{\leq 0} := -\mathcal{J}_{\geq 0}, \qquad \mathcal{J}_{>0} := \mathcal{J} \cap \mathbb{N}^*, \quad \mathcal{J}_{<0} := -\mathcal{J}_{>0},$
- $\mathcal{K} := [\![0, k_{\max} - 1]\!], \quad \overline{\mathcal{K}} := [\![0, k_{\max}]\!],$
- $\forall k \in \overline{\mathcal{K}}, \quad t_k := k\Delta t,$
- $\mathcal{E} := \mathcal{I} \times \mathcal{J}, \qquad \mathcal{E}_{\mathrm{ext}} := \overline{\mathcal{I}} \times \mathcal{J}, \qquad \overline{\mathcal{E}} := \left(\overline{\mathcal{I}} \times \mathcal{J}\right) \cup \left(\mathcal{I} \times \overline{\mathcal{J}}\right).$

Because of the reset mechanism, we choose Δx so that it is possible to define an index $i_{\mathrm{R}} \in \mathcal{I}$ such that $x_{i_{\mathrm{R}}} = u_{\mathrm{R}}$. Our scheme will also ask for special consecutive-in-j interior values. To be able to implement all the above, we therefore assume $i_{\mathrm{F}} \geq 2$ and $j_{\max} \geq 2$. We now define a space of admissible functions on the extended grid $\mathcal{E}_{\mathrm{ext}}$:

Definition 2. We define the space $\ell^1_+\left(\mathcal{E}_{\mathrm{ext}}\right)$ to be the set of functions F in $\mathbb{R}_+^{\mathcal{E}_{\mathrm{ext}}}$ verifying

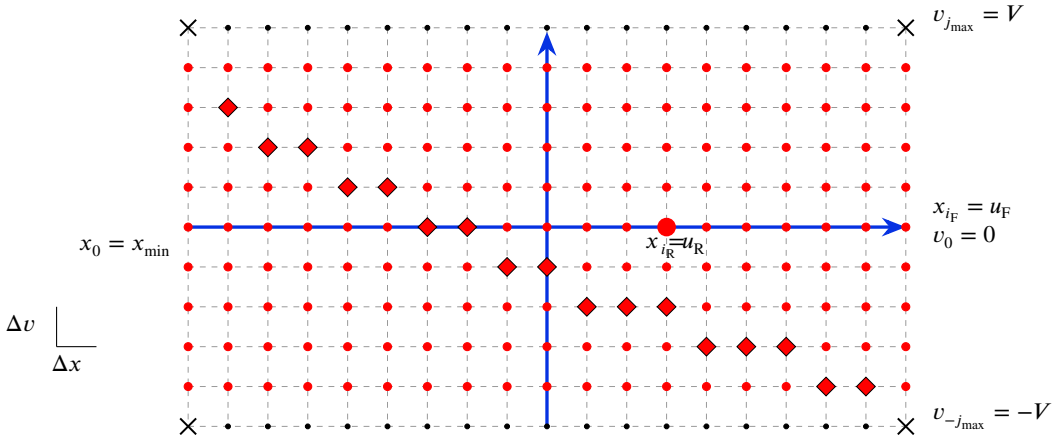
$$\|F\|_{\ell^1_+(\mathcal{E}_{\mathrm{ext}})} := \sum_{(i,j)\in\mathcal{E}_{\mathrm{ext}}} F_{i,j} < +\infty. \tag{22}$$

For any F in $\ell^1_+\left(\mathcal{E}_{\mathrm{ext}}\right)$, we define its mass $\mathscr{M}(F)$ through the formula:

$$\mathscr{M}(F) := \Delta x \Delta v \sum_{(i,j)\in\mathcal{E}_{\mathrm{ext}}} F_{i,j}. \tag{23}$$

Of course, since $\mathcal{E}_{\mathrm{ext}}$ is finite, condition (22) is automatically verified; the notation is introduced to make the discrete estimates more transparent. An interesting extension would be to consider $V = +\infty$: in this context, the condition would gain its full mathematical relevance.

Figure 6: Nodal points (x_i, v_j) indexed by $\overline{\mathcal{E}}$; the four corner points of $\overline{\mathcal{I}} \times \overline{\mathcal{J}}$ are excluded from $\overline{\mathcal{E}}$ and are marked with crosses $\times$. The red circular nodes $\bullet$ correspond to the extended grid $\mathcal{E}_{\text{ext}}$, on which the physical properties are studied. For some fixed arbitrary $k \in \mathcal{K}$, for pedagogic purposes, possible locations of nodes corresponding to the critical indexes 24 $j_c(i,k), i \in \mathcal{I}$ are indicated by $\blacklozenge$, while the remaining black nodes $\bullet$ come from $\overline{\mathcal{E}} \setminus \mathcal{E}_{\text{ext}}$.



The vector field μ corresponding to the drift is discretized with the following formulas, for (i, j, k) in $\overline{\mathcal{E}} \times \mathcal{K}$, and $N^k \in \mathbb{R}$ to be defined later:

$$\left(\mu_1^k\right)_{i,j} := v_j$$

$$\left(\mu_2^k\right)_{i,j} := -\frac{v_j}{\tau} - {\omega_0}^2 x_i + b(N^k + \nu_{\text{ext}}).$$

The sign of μ_2 will be of great importance in what follows. Assuming that the discrete drift remains vertically confining on the interior velocity grid $\mathcal{J}$, as will be specified later in Assumption (2), the vertical drift changes sign at a unique critical index for each fixed pair (i, k). This motivates the following definition.

Definition 3. For all i in $\mathcal{I}$, for all k in $\mathcal{K}$, there exists a unique index in $\mathcal{J}$, denoted $j_c(i,k)$, such that $(\mu_2)^k_{i,j_c(i,k)} \geq 0$ and $(\mu_2)^k_{i,j_c(i,k)+1} < 0$. Equivalently,

$$j_c(i,k) := \left\lfloor \frac{\tau\left(b(N^k + \nu_{\text{ext}}) - \omega_0^2 x_i\right)}{\Delta v} \right\rfloor. \tag{24}$$

Since j_c is the index where the sign change happens, $(\mu_2)^k_{i,j_c(i,k)}$ and $(\mu_2)^k_{i,j_c(i,k)+1}$ are small in absolute value compared to the others $(\mu_2)^k_{i,j}$. More precisely:

$$-\frac{\Delta v}{\tau} \leq (\mu_2)^k_{i,j_c(i,k)+1} < 0 \leq (\mu_2)^k_{i,j_c(i,k)} < \frac{\Delta v}{\tau}. \tag{25}$$

This motivates the introduction of the following critical-index correction, which is expected to vanish as $\Delta v \to 0$ under suitable stability properties of the scheme:

Definition 4. For all i in $\mathcal{I}$, for all k in $\mathcal{K}$, we define

$$e_i^k := (\mu_2^k)_{i,j_c(i,k)} f^k_{i,j_c(i,k)+1} - (\mu_2^k)_{i,j_c(i,k)+1} f^k_{i,j_c(i,k)}. \tag{26}$$

With this setup in place, to maintain control of non-negativity and mass, we discretize the transport part in an upwind spirit, using values located upstream with respect to the characteristic flow. We now define the corresponding discrete operators. For any real number α, we denote by $\alpha^+ := \max(\alpha, 0)$ (respectively $\alpha^- := \max(-\alpha, 0)$) its positive (respectively negative) part.

Definition 5. For F in $\ell^1_+\left(\mathcal{E}_{\text{ext}}\right)$, we define the upstream discretizations of the space derivative $\frac{\partial}{\partial x}$ by, for all j in $\mathcal{J}$:

$$\forall i \in [\![0, i_{\text{F}} - 1]\!], \quad (D_x^+ F)_{i,j} := \frac{F_{i+1,j} - F_{i,j}}{\Delta x},$$

$$(D_x^+ F)_{i_{\text{F}},j} := 0,$$

$$\forall i \in [\![1, i_{\text{F}}]\!], \quad (D_x^- F)_{i,j} := \frac{F_{i,j} - F_{i-1,j}}{\Delta x},$$

$$(D_x^- F)_{0,j} := 0,$$

for all (i, j, k) in $\mathcal{E}_{\text{ext}} \times \mathcal{K}$,

$$\left(\mu_1 D_x F\right)^k_{i,j} := \left(\left(\mu_1^k\right)_{i,j}\right)^+ (D_x^- F)_{i,j} - \left(\left(\mu_1^k\right)_{i,j}\right)^- (D_x^+ F)_{i,j} = v_j^+ (D_x^- F)_{i,j} - v_j^- (D_x^+ F)_{i,j}.$$

The main originality of the scheme lies in the use of the critical indices to adapt the discretization of the velocity derivative:

Definition 6. For F in $\ell^1_+\left(\mathcal{E}_{\text{ext}}\right)$, we define the upstream discretizations of the velocity derivative $\frac{\partial}{\partial v}$ by introducing, for all (i, j) in $\mathcal{E}$,

$$(D_v^+ F)_{i,j} := \frac{F_{i,j+1} - F_{i,j}}{\Delta v},$$

$$(D_v^- F)_{i,j} := \frac{F_{i,j} - F_{i,j-1}}{\Delta v},$$

as well as: for all (i, j, k) in $\mathcal{E} \times \mathcal{K}$, $j \notin \{j_{\text{c}}(i,k), j_{\text{c}}(i,k) + 1\}$,

$$(\mu_2 \mathscr{D}_v F)^k_{i,j} := \left(\mu_2^k\right)^+_{i,j} (D_v^- F)_{i,j} - \left(\mu_2^k\right)^-_{i,j} (D_v^+ F)_{i,j},$$

and

$$(\mu_2 \mathscr{D}_v F)^k_{i,j_{\text{c}}(i,k)} := \left(\mu_2^k\right)_{i,j_{\text{c}}(i,k)} (D_v^- F)_{i,j_{\text{c}}(i,k)} - (\mu_2)^k_{i,j_{\text{c}}(i,k)+1} \frac{F_{i,j_{\text{c}}(i,k)}}{\Delta v},$$

$$(\mu_2 \mathscr{D}_v F)^k_{i,j_{\text{c}}(i,k)+1} := \left(\mu_2^k\right)_{i,j_{\text{c}}(i,k)+1} (D_v^+ F)_{i,j_{\text{c}}(i,k)+1} + (\mu_2)^k_{i,j_{\text{c}}(i,k)} \frac{F_{i,j_{\text{c}}(i,k)+1}}{\Delta v}.^2 \tag{27}$$

On the sides of the extended grid, for all j in $\mathcal{J}$,

$$(\mu_2 \mathscr{D}_v F)^k_{0,j} := (\mu_2 \mathscr{D}_v F)^k_{i_{\text{F}},j} := 0.$$

Definition 7. For F in $\ell^1_+\left(\mathcal{E}_{\text{ext}}\right)$, the discretization on $\mathcal{E}_{\text{ext}}$ of the second order velocity derivative is given by, for all (i, j) in $\mathcal{E}$:

$$(D_v^2 F)_{i,j} := \frac{F_{i,j+1} - 2F_{i,j} + F_{i,j-1}}{\Delta v^2},$$

and for all j in $\mathcal{J}$,

$$(D_v^2 F)_{0,j} := (D_v^2 F)_{i_{\text{F}},j} := 0.$$

[2] The case for discretization 27 being seen as a reasonable approximation of the continuous operator can be made thanks to inequality 25: the terms on the far right of both equations, seemingly superfluous, are well controlled for sufficiently well-behaved solutions.

We also introduce the discrete counterpart of the continuous coefficient $-\frac{\partial}{\partial v}\mu_2 = 1/\tau$, which appears when the conservative term $\frac{\partial}{\partial v}(\mu_2 f)$ is expanded:

Definition 8. For all (i,j) in $\mathcal{E}_{\text{ext}}$, we define the discrete damping coefficient by:

$$d_{i,j} := \begin{cases} \dfrac{1}{\tau} & \text{if } i \in \mathcal{I}, \\ \\ 0 & \text{otherwise.} \end{cases} \tag{28}$$

3.3. Scheme definition

So as not to have to deal with the potentially problematic outflow vertical boundary, we want to translate Assumption (1) in a precise manner in our numerical setting. Denoting

$$X := \max\left(u_{\text{F}}, |x_{\min}|\right), \tag{29}$$

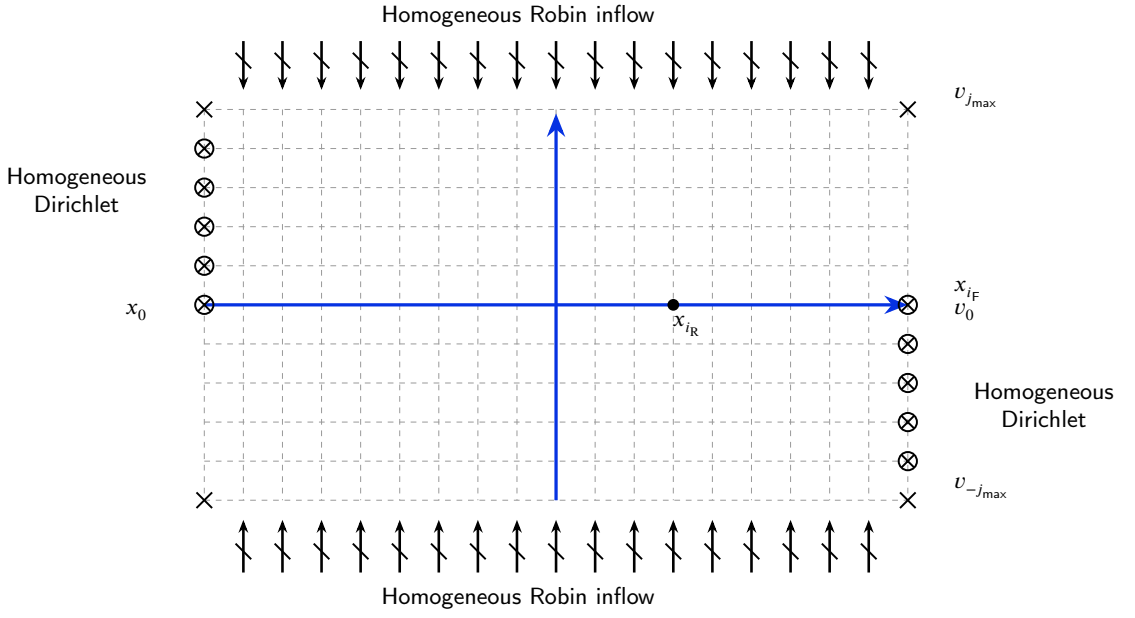
we will thus work for the rest of the paper around the following dynamical condition, for all k in $\mathcal{K}$:

Assumption 2.

$$V > \tau\left(X\omega_0^2 + |b|\left(\nu_{\text{ext}} + N^k\right)\right) + \Delta v.$$

We can immediately remark that, for all $i \in \overline{\mathcal{I}}$, we get $(\mu_2^k)_{i,j_{\max}-1}$ and $(\mu_2^k)_{i,j_{\max}}$ negative as well as $(\mu_2^k)_{i,1-j_{\max}}$ and $(\mu_2^k)_{i,-j_{\max}}$ positive. Thus, if we define the behavior at the boundary thanks to these drift vectors, we have the totality of the upper and lower extended grid being an *inflow* boundary as we had with the simplified Problem (21), this setting being represented in Figure 7. On this figure the full grid $\overline{\mathcal{E}}$ is shown, we thus can see the interior grid $\mathcal{E}$, as well as the associated horizontal and vertical boundary conditions. The four corner points are marked with a cross $\times$ since they don't belong to $\overline{\mathcal{E}}$.

Figure 7: Full grid $\overline{\mathcal{E}}$ with boundary conditions for scheme (30).



Meanwhile, the discrete reset distribution satisfies

$$\rho_{i,j} \geq 0, \qquad \rho_{i,j} = 0 \quad \text{on } \mathcal{E}_{\text{ext}} \setminus \mathcal{E}, \qquad \Delta x \Delta v \sum_{(i,j)\in\mathcal{E}} \rho_{i,j} = 1.$$

Starting from a discrete initial datum $(f^0_{i,j})_{(i,j)\in\mathcal{E}_{\text{ext}}} \in \ell^1_+(\mathcal{E}_{\text{ext}})$, chosen discretization of the initial boundary value problem (21) is given below via our main semi-implicit upwind scheme of interest defined by, for all $k \in \mathcal{K}$:

Semi-implicit Euler step:

$$\forall (i,j)\in\mathcal{E}_{\text{ext}},\quad \frac{f^{k+1}_{i,j}-f^k_{i,j}}{\Delta t} + (\mu_1 D_x f^k)^k_{i,j} + (\mu_2 \mathscr{D}_v f^k)^k_{i,j} - d_{i,j} f^k_{i,j} - (a_0 + a_1 N^k)(D_v^2 f^{k+1})_{i,j} = N^k \rho_{i,j}, \tag{30a}$$

Numerical activity:

$$N^k := \sum_{j=1}^{j_{\max}-1} v_j f^k_{i_{\text{F}},j}\Delta v - \sum_{j=1-j_{\max}}^{-1} v_j f^k_{0,j}\Delta v, \tag{30b}$$

Boundary conditions:

Homogeneous Robin:

$$\begin{aligned}&(\mu_2^k)_{i,j_{\max}-1} f^k_{i,j_{\max}} - (a_0 + a_1 N^k)(D_v^+ f^{k+1})_{i,j_{\max}-1} = 0,\\ &(\mu_2^k)_{i,1-j_{\max}} f^k_{i,-j_{\max}} - (a_0 + a_1 N^k)(D_v^- f^{k+1})_{i,1-j_{\max}} = 0, \quad \text{for } i \in \mathcal{I},\end{aligned} \tag{30c}$$

Homogeneous Dirichlet inflow:

$$f^{k+1}_{i,j} = 0, \qquad \text{if } \big(i = i_{\text{F}} \text{ and } j \in \mathcal{J}_{\le 0}\big) \text{ or } \big(i = 0 \text{ and } j \in \mathcal{J}_{\ge 0}\big), \tag{30d}$$

A few observations can be made:

- The indices $j_{\max}$ and $-j_{\max}$ are there to construct *ghost points* which allow to write the homogeneous Robin conditions (30c) in an elegant way. They are auxiliary values, introduced only to encode the vertical Robin conditions and not counted as physical density values nor needed for the discrete-in-time evolution of scheme (30). For example, for $i \in \mathcal{I}, j = j_{\max}-1$, 30c can be rewritten, when the adjacent node is not critical:

$$\begin{aligned}&\frac{f^{k+1}_{i,j_{\max}-1} - f^k_{i,j_{\max}-1}}{\Delta t} + v_{j_{\max}-1}\frac{f^k_{i,j_{\max}-1} - f^k_{i-1,j_{\max}-1}}{\Delta x}\\ &\quad - (\mu_2^k)_{i,j_{\max}-1}\frac{f^k_{i,j_{\max}-1}}{\Delta v} - \frac{f^k_{i,j_{\max}-1}}{\tau} + (a_0 + a_1 N^k)\frac{f^{k+1}_{i,j_{\max}-1} - f^{k+1}_{i,j_{\max}-2}}{\Delta v^2} = N^k \rho_{i,j_{\max}-1}.\end{aligned} \tag{31}$$

- As a consequence, it follows directly from the scheme's definition that one can obtain f^{k+1} on the extended grid $\mathcal{E}_{\text{ext}}$ as soon as $f^k \ge 0$ is known.

- The physical conditions on the initial datum of Problem (21) can be interpreted in a very natural manner in the form:

$$\forall (i,j)\in\mathcal{E}_{\text{ext}},\quad f^0_{i,j} \ge 0, \qquad \Delta x \Delta v \sum_{(i,j)\in\mathcal{E}_{\text{ext}}} f^0_{i,j} = 1. \tag{32}$$

  We also enforce the following condition which is physically meaningful and makes formula (30b) coherent:

$$f^0_{i,j} = 0, \qquad \text{if } \big(i = i_{\text{F}} \text{ and } j \in \mathcal{J}_{\le 0}\big) \text{ or } \big(i = 0 \text{ and } j \in \mathcal{J}_{\ge 0}\big). \tag{33}$$

- Using the definition of the operators we just gave in this subsection, one can precisely write the formulas for the numerical traces on the sides of the domain:

$$\forall j \in \mathcal{J}_{>0}, \qquad \frac{f^{k+1}_{i_{\text{F}},j} - f^k_{i_{\text{F}},j}}{\Delta t} + v_j \frac{f^k_{i_{\text{F}},j} - f^k_{i_{\text{F}}-1,j}}{\Delta x} = 0,$$

$$\forall j \in \mathcal{J}_{<0}, \qquad \frac{f_{0,j}^{k+1} - f_{0,j}^{k}}{\Delta t} + v_j \frac{f_{1,j}^{k} - f_{0,j}^{k}}{\Delta x} = 0, \tag{34}$$

Formula (34) shows that, on the horizontal edges, we get the trace via a simple transport equation in x, as in the Boltzmann equation setting [63].[3]

- The Robin boundary conditions (30c), show a discrepancy in discrete times, some terms being taken at time k and another one at time $k+1$; this is coherent with Euler step (30a) being semi-implicit. Since when the discrete steps go to 0, times k and $k+1$ get infinitely closer to one another, the continuous Robin boundary conditions are actually expected to be recovered for well-behaved solutions.

Before moving forward, let us summarize the practical meaning of scheme (30). Assume that f^k is known on the extended grid. First, the discrete activity N^k is computed from the boundary flux formula. This fixes the coefficients $a_0 + a_1 N^k$ and the drift in the v direction at time t_k. The transport terms in x and v, the reset contribution, and the boundary corrections are then treated explicitly. Finally, the vertical diffusion is treated implicitly, which amounts, for each fixed x_i, to solving a tridiagonal linear system in the velocity variable. The result is the next density f^{k+1}.

3.4. Properties of the scheme

Let us now prove rigorously the conservation properties of our scheme.

3.4.1. Non-negativity preservation

One can first prove a non-negativity preservation principle:

Property 3. Provided Assumption 2 and the following CFL-type condition

$$\Delta t \leq \frac{1}{V\left(\frac{1}{\Delta x} + \frac{1}{\tau \Delta v}\right) + X\frac{\omega_0^2}{\Delta v} + \frac{|b|(N^k + \nu_{\text{ext}})}{\Delta v}}, \tag{35}$$

are satisfied at every time step k in $\mathcal{K}$, the scheme (30) preserves the non-negativity of the initial condition:

$$\min_{(i,j)\in\mathcal{E}_{\text{ext}}} f_{i,j}^0 \geq 0 \implies \min_{(i,j,k)\in\mathcal{E}_{\text{ext}}\times\overline{\mathcal{K}}} f_{i,j}^k \geq 0. \tag{36}$$

Proof. Let us assume $\min_{(i,j)\in\mathcal{E}_{\text{ext}}} f_{i,j}^0 \geq 0$. For the rest of the proof we will denote, for $k \in \overline{\mathcal{K}}$:

$$\mathsf{m}^k := \min_{(i,j)\in\mathcal{E}_{\text{ext}}} f_{i,j}^k. \tag{37}$$

We proceed by induction, assuming condition (35) and

$$\min_{(i,j)\in\mathcal{E}_{\text{ext}}} f_{i,j}^k \geq 0 \tag{38}$$

are verified for some fixed $k \in \mathcal{K}$. We can notice that $N^k \geq 0$ since $f^k \geq 0$ on the extended grid $\mathcal{E}_{\text{ext}}$, by definition of the discrete activity 30b. For the sake of brevity, we assume here that the Robin adjacent node is not one of the two critical nodes (the complementary case being easily treated with the same technique as below, by using the critical-index formula (27) and the homogeneous Robin conditions 30c).

1. Let us first assume that m^{k+1} is attained strictly at the interior of $\mathcal{E}_{\text{ext}}$, by which we mean $(i,j) \in \mathcal{I} \times [\![2 - j_{\max}, j_{\max} - 2]\!]$, denoting i_{m}^{k+1} and j_{m}^{k+1} the smallest values of i and j such that m^{k+1} is attained. The case $j_{\mathsf{m}}^{k+1} \notin \{j_{\mathrm{c}}(i_{\mathsf{m}}^{k+1}, k), j_{\mathrm{c}}(i_{\mathsf{m}}^{k+1}, k) + 1\}$ is classical, the non-negativity of the right-hand side added to the upwind scheme giving the result.

[3] More elaborate ways of building boundary values in numerical schemes for kinetic equations have already been introduced (notably in [32]), the study of the compatibility of such computations with the mass conservation and non-negativity preservation we aim for here could be the topic of interesting developments.

Now if $j_{\mathsf{m}}^{k+1} \in \{j_{\mathrm{c}}(i_{\mathsf{m}}^{k+1}, k), j_{\mathrm{c}}(i_{\mathsf{m}}^{k+1}, k) + 1\}$, using the Euler step (30a) for the adapted operators 27, we get, in the case $j_{\mathsf{m}}^{k+1} = j_{\mathrm{c}}(i_{\mathsf{m}}^{k+1}, k)$:

$$
\begin{aligned}
\mathsf{m}^{k+1} - \mathsf{m}^k \geq & \left(f^k_{i_{\mathsf{m}}^{k+1}, j_{\mathsf{m}}^{k+1}} - \mathsf{m}^k \right) \left[1 - \Delta t \left(\frac{v^+_{j_{\mathsf{m}}^{k+1}} + v^-_{j_{\mathsf{m}}^{k+1}}}{\Delta x} + \frac{\left((\mu_2)^k_{i_{\mathsf{m}}^{k+1}, j_{\mathsf{m}}^{k+1}} \right)^+ + \left((\mu_2)^k_{i_{\mathsf{m}}^{k+1}, j_{\mathsf{m}}^{k+1}} \right)^-}{\Delta v} \right) \right] \\
& + \Delta t \frac{f^k_{i_{\mathsf{m}}^{k+1}, j_{\mathsf{m}}^{k+1}}}{\tau} - \Delta t v^+_{j_{\mathsf{m}}^{k+1}} \frac{\mathsf{m}^k - f^k_{i_{\mathsf{m}}^{k+1}-1, j_{\mathsf{m}}^{k+1}}}{\Delta x} + \Delta t v^-_{j_{\mathsf{m}}^{k+1}} \frac{f^k_{i_{\mathsf{m}}^{k+1}+1, j_{\mathsf{m}}^{k+1}} - \mathsf{m}^k}{\Delta x} \\
& - \Delta t \left((\mu_2)^k_{i_{\mathsf{m}}^{k+1}, j_{\mathsf{m}}^{k+1}} \right)^+ \frac{\mathsf{m}^k - f^k_{i_{\mathsf{m}}^{k+1}, j_{\mathsf{m}}^{k+1}-1}}{\Delta v} + \Delta t \left((\mu_2)^k_{i_{\mathsf{m}}^{k+1}, j_{\mathsf{m}}^{k+1}} \right)^- \frac{f^k_{i_{\mathsf{m}}^{k+1}, j_{\mathsf{m}}^{k+1}+1} - \mathsf{m}^k}{\Delta v} \\
& + \Delta t \, f^k_{i_{\mathsf{m}}^{k+1}, j_{\mathsf{m}}^{k+1}} \frac{(\mu_2)^k_{i_{\mathsf{m}}^{k+1}, j_{\mathsf{m}}^{k+1}+1}}{\Delta v} \\
\geq & \left(f^k_{i_{\mathsf{m}}^{k+1}, j_{\mathsf{m}}^{k+1}} - \mathsf{m}^k \right) \left[1 - \Delta t \left(|v_{j_{\mathsf{m}}^{k+1}}| \left(\frac{1}{\Delta x} + \frac{1}{\tau \Delta v} \right) + \frac{\omega_0^2 |x_{i_{\mathsf{m}}^{k+1}}| + |b|(N^k + \nu_{\mathrm{ext}})}{\Delta v} \right) \right] \\
& + \Delta t \, f^k_{i_{\mathsf{m}}^{k+1}, j_{\mathsf{m}}^{k+1}} \left(\frac{1}{\tau} + \frac{(\mu_2)^k_{i_{\mathsf{m}}^{k+1}, j_{\mathrm{c}}(i_{\mathsf{m}}^{k+1}, k)+1}}{\Delta v} \right) \\
\geq & \, 0,
\end{aligned}
$$

the last inequality coming from (25). The case $j_{\mathsf{m}}^{k+1} = j_{\mathrm{c}}(i_{\mathsf{m}}^{k+1}, k) + 1$ is treated in an analogous manner.

2. Let us now assume that m^{k+1} is attained for an $(i, j) \in \mathcal{I} \times \{j_{\max} - 1\}$. Using the Robin boundary condition (30c) in the equation defining the scheme gives equation (31). Since $N^k \rho_{i_{\mathsf{m}}^{k+1}, j_{\max}-1} \geq 0$, one gets

$$
\begin{aligned}
\mathsf{m}^{k+1} & \geq f^k_{i_{\mathsf{m}}^{k+1}, j_{\max}-1} - \Delta t \, v_{j_{\max}-1} \frac{f^k_{i_{\mathsf{m}}^{k+1}, j_{\max}-1} - f^k_{i_{\mathsf{m}}^{k+1}-1, j_{\max}-1}}{\Delta x} + \Delta t \left(\frac{(\mu_2^k)_{i_{\mathsf{m}}^{k+1}, j_{\max}-1}}{\Delta v} + \frac{1}{\tau} \right) f^k_{i_{\mathsf{m}}^{k+1}, j_{\max}-1} \\
& = \left[1 - \Delta t \frac{v_{j_{\max}-1}}{\Delta x} + \Delta t \left(\frac{(\mu_2^k)_{i_{\mathsf{m}}^{k+1}, j_{\max}-1}}{\Delta v} + \frac{1}{\tau} \right) \right] f^k_{i_{\mathsf{m}}^{k+1}, j_{\max}-1} + \Delta t \frac{v_{j_{\max}-1}}{\Delta x} f^k_{i_{\mathsf{m}}^{k+1}-1, j_{\max}-1}.
\end{aligned}
$$

Since the CFL condition (35) implies

$$
1 - \Delta t \frac{v_{j_{\max}-1}}{\Delta x} + \Delta t \left(\frac{(\mu_2^k)_{i_{\mathsf{m}}^{k+1}, j_{\max}-1}}{\Delta v} + \frac{1}{\tau} \right) \geq 0,
$$

by the induction hypothesis, $\mathsf{m}^{k+1} \geq 0$.
The case $(i, j) \in \mathcal{I} \times \{1 - j_{\max}\}$ is treated in the same way, using the lower Robin boundary condition.

3. If $(i_{\mathsf{m}}^{k+1}, j_{\mathsf{m}}^{k+1}) \in \left(\{0\} \times \mathcal{J}_{\geq 0} \right) \cup \left(\{i_{\mathrm{F}}\} \times \mathcal{J}_{\leq 0} \right)$, then because of the Dirichlet conditions (30d), $\mathsf{m}^{k+1} = 0$, and the desired non-negativity follows. Now if $(i_{\mathsf{m}}^{k+1}, j_{\mathsf{m}}^{k+1}) \in \left(\{0\} \times \mathcal{J}_{<0} \right) \cup \left(\{i_{\mathrm{F}}\} \times \mathcal{J}_{>0} \right)$, we use the explicit trace step (34) which gives us, for the case $\{i_{\mathrm{F}}\} \times \mathcal{J}_{>0}$:

$$
\begin{aligned}
\mathsf{m}^{k+1} - \mathsf{m}^k & \geq \left(f^k_{i_{\mathrm{F}}, j_{\mathsf{m}}^{k+1}} - \mathsf{m}^k \right) \left[1 - \Delta t \frac{v_{j_{\mathsf{m}}^{k+1}}}{\Delta x} \right] - \Delta t \, v_{j_{\mathsf{m}}^{k+1}} \frac{\mathsf{m}^k - f^k_{i_{\mathrm{F}}-1, j_{\mathsf{m}}^{k+1}}}{\Delta x} \\
& \geq \left(f^k_{i_{\mathrm{F}}, j_{\mathsf{m}}^{k+1}} - \mathsf{m}^k \right) \left[1 - \Delta t \frac{v_{j_{\mathsf{m}}^{k+1}}}{\Delta x} \right],
\end{aligned}
$$

and thus our result. The case $\{0\} \times \mathcal{J}_{\leq 0}$ being treated in the same way, this finishes the proof.

□

Remark 3.3. The CFL type condition (35) can slightly be relaxed when it comes to preservation of non-negativity; we still chose this presentation since it was easier to read and implement than the best condition we managed to discover.

Remark 3.4. Assumption (2) has a direct effect on Condition 35. Indeed, Assumption (2) requires the velocity cutoff V to be large enough for the mass-preservation argument to be valid. For a fixed velocity step Δv, increasing V amounts to increasing the number of grid points in the v-direction, of order $V/\Delta v$. Since this factor enters the CFL restriction in Condition 35, the non-negativity constraint becomes more restrictive as the velocity grid becomes larger. Thus, increasing the size of the v-grid in order to preserve mass forces one to choose a sufficiently small time step Δt in order to preserve non-negativity throughout the execution of the scheme.

3.4.2. Mass conservation

We introduce a discrete integration by parts lemma, proved in Appendix B:

Lemma 1 (Discrete upwind integration by parts)**.** Let f^k be in $\ell^1_+(\mathcal{E}_{\text{ext}})$, and let us suppose that Assumption (2) is verified. Then the following upwind discrete integration by parts formula holds:

$$\begin{aligned}\sum_{i=1}^{i_{\text{F}}-1}\sum_{j=1-j_{\max}}^{j_{\max}-1}\left[\left(\mu_2\right)^k_{i,j}\right]^+\left(D_v^- f^k\right)_{i,j} - \left[\left(\mu_2\right)^k_{i,j}\right]^-\left(D_v^+ f^k\right)_{i,j}\\ = \frac{1}{\tau}\sum_{i=1}^{i_{\text{F}}-1}\sum_{j=1-j_{\max}}^{j_{\max}-1} f^k_{i,j} - \frac{1}{\Delta v}\sum_{i=1}^{i_{\text{F}}-1}\left[e^k_i + \left[\left(\mu_2\right)^k_{i,1-j_{\max}}\right]^+ f^k_{i,-j_{\max}}\right.\\ \left. + \left[\left(\mu_2\right)^k_{i,j_{\max}-1}\right]^- f^k_{i,j_{\max}}\right], \quad (39)\end{aligned}$$

where, for all $(i,k)\in\mathcal{I}\times\mathcal{K}$, $j_{\text{c}}(i,k)$ is defined as in 24 and e^k_i as in 26.

We can then prove the discrete mass preservation result announced in the introduction:

Property 4. Under the assumptions of the preceding property, the scheme (30) is mass preserving.

Proof. Let us consider $f^0\in\ell^1_+(\mathcal{E}_{\text{ext}})$, and $(f^k)_{k\in\overline{\mathcal{K}}}$ the sequence in $\left(\ell^1_+(\mathcal{E}_{\text{ext}})\right)^{k_{\max}+1}$ obtained through the application of scheme (30) to f^0.

By definition of $\ell^1_+(\mathcal{E}_{\text{ext}})$, we can then introduce for the purpose of this proof, for all k in $\overline{\mathcal{K}}$, the interior mass m^k and the extended mass M^k:

$$m^k := \Delta x\Delta v\sum_{(i,j)\in\mathcal{E}} f^k_{i,j}, \qquad M^k := \mathscr{M}(f^k),$$

with $\mathscr{M}$ defined in equation (23).

For a given k in $\mathcal{K}$ we sum formula (30a) over the interior grid $\mathcal{E}$ and multiply it by $\Delta x\Delta v$, obtaining:

$$\begin{aligned}N^k = \frac{m^{k+1}-m^k}{\Delta t} + \Delta v\sum_{j=1}^{j_{\max}-1} v_j(f^k_{i_{\text{F}}-1,j} - f^k_{0,j}) + \Delta v\sum_{j=1-j_{\max}}^{-1} v_j(f^k_{i_{\text{F}},j} - f^k_{1,j}) + \Delta x\sum_{(i,j)\in\mathcal{E}}(\mu_2^k)^+_{i,j}(f^k_{i,j} - f^k_{i,j-1})\\ - \Delta x\sum_{(i,j)\in\mathcal{E}}(\mu_2^k)^-_{i,j}(f^k_{i,j+1} - f^k_{i,j}) - \Delta x\sum_{i=1}^{i_{\text{F}}-1}(\mu_2^k)_{i,j_{\text{c}}(i,k)+1} f^k_{i,j_{\text{c}}(i,k)} + \Delta x\sum_{i=1}^{i_{\text{F}}-1}(\mu_2^k)_{i,j_{\text{c}}(i,k)} f^k_{i,j_{\text{c}}(i,k)+1}\\ - \frac{m^k}{\tau} - \Delta x(a_0 + a_1 N^k)\sum_{i\in\mathcal{I}}\frac{f^{k+1}_{i,j_{\max}} - f^{k+1}_{i,j_{\max}-1}}{\Delta v} - \frac{f^{k+1}_{i,1-j_{\max}} - f^{k+1}_{i,-j_{\max}}}{\Delta v},\end{aligned}$$

thanks to $(\rho_{i,j})_{i,j}$ having all of its (unit) mass concentrated inside the interior grid (i.e. $\Delta x\Delta v\sum_{(i,j)\in\mathcal{E}}\rho_{i,j} = 1$).

Now using the no-influx Dirichlet boundary conditions on the inflow sides of the domain 30d, as well as Lemma 1, we get:

$$N^k = \frac{m^{k+1}-m^k}{\Delta t} + \Delta v \sum_{j=1}^{j_{\max}-1} v_j f^k_{i_{\mathrm{F}}-1,j} - \Delta v \sum_{j=1-j_{\max}}^{-1} v_j f^k_{1,j} + \Delta x \sum_{i=1}^{i_{\mathrm{F}}-1} \left[-\left[(\mu_2)^k_{i,1-j_{\max}}\right]^+ f^k_{i,-j_{\max}} - \left[(\mu_2)^k_{i,j_{\max}-1}\right]^- f^k_{i,j_{\max}} \right] - \Delta x(a_0 + a_1 N^k) \sum_{i=1}^{i_{\mathrm{F}}-1} \left(\frac{f^{k+1}_{i,j_{\max}} - f^{k+1}_{i,j_{\max}-1}}{\Delta v} - \frac{f^{k+1}_{i,1-j_{\max}} - f^{k+1}_{i,-j_{\max}}}{\Delta v} \right).$$

Adding on both sides $\frac{\Delta x \Delta v}{\Delta t}\left(\sum_{j=1}^{j_{\max}-1} f^{k+1}_{i_{\mathrm{F}},j} - f^k_{i_{\mathrm{F}},j} + \sum_{j=1-j_{\max}}^{-1} f^{k+1}_{0,j} - f^k_{0,j} \right)$ to make the total mass appear, we get:

$$\frac{\Delta x \Delta v}{\Delta t}\left(\sum_{j=1}^{j_{\max}-1} f^{k+1}_{i_{\mathrm{F}},j} - f^k_{i_{\mathrm{F}},j} + \sum_{j=1-j_{\max}}^{-1} f^{k+1}_{0,j} - f^k_{0,j} \right) + \Delta v \sum_{j=1}^{j_{\max}-1} v_j \left(f^k_{i_{\mathrm{F}},j} - f^k_{i_{\mathrm{F}}-1,j} \right) - \Delta v \sum_{j=1-j_{\max}}^{-1} v_j \left(f^k_{0,j} - f^k_{1,j} \right)$$
$$= \frac{M^{k+1}-M^k}{\Delta t} + \Delta x \sum_{i=1}^{i_{\mathrm{F}}-1} \left[-\left[(\mu_2)^k_{i,1-j_{\max}}\right]^+ f^k_{i,-j_{\max}} - \left[(\mu_2)^k_{i,j_{\max}-1}\right]^- f^k_{i,j_{\max}} \right] - \Delta x(a_0 + a_1 N^k) \sum_{i=1}^{i_{\mathrm{F}}-1} \left(\frac{f^{k+1}_{i,j_{\max}} - f^{k+1}_{i,j_{\max}-1}}{\Delta v} - \frac{f^{k+1}_{i,1-j_{\max}} - f^{k+1}_{i,-j_{\max}}}{\Delta v} \right).$$

Using the numerical trace relations (34), the lateral transport terms are converted into the time variation of the boundary mass. We obtain

$$\frac{M^{k+1}-M^k}{\Delta t} = \Delta x \sum_{i=1}^{i_{\mathrm{F}}-1} \left[\left[(\mu_2)^k_{i,1-j_{\max}}\right]^+ f^k_{i,-j_{\max}} + \left[(\mu_2)^k_{i,j_{\max}-1}\right]^- f^k_{i,j_{\max}} + (a_0 + a_1 N^k)\left(\frac{f^{k+1}_{i,j_{\max}} - f^{k+1}_{i,j_{\max}-1}}{\Delta v} - \frac{f^{k+1}_{i,1-j_{\max}} - f^{k+1}_{i,-j_{\max}}}{\Delta v} \right) \right].$$

We can then take advantage of the upwind numerical Robin boundary condition (30c) to obtain:

$$M^{k+1} = M^k$$

and thus our result. □

Remark 3.5. The conserved quantity is the extended mass, which includes the lateral boundary values entering the numerical activity. This is natural for the present semi-implicit scheme: mass reaching the lateral boundary at time t_k contributes to N^k and is reinjected through the source term, while the corresponding boundary values remain part of the discrete probability mass during the update.

4. Numerical experiments

The reader is referred to the accompanying GitHub repository, which contains scripts used to produce the experiments presented in this section, as well as additional material such as figures or videos illustrating the observed phenomena. An archived and citable version of the repository is also available on Zenodo [69].

Unless specifically mentioned otherwise, all the tests below involving the PDE will have the following parameters in common: the maximum voltage value on the x grid is the threshold value $u_{\mathrm{F}} = x_{i_{\mathrm{F}}} = 9$, the right-hand side is

discretized via a discrete Maxwellian centered at $(u_R, 0)$, with standard deviation $\sigma_\rho = 10^{-3}$, multiplied by $\mathbf{1}_{\mathcal{E}}(i,j)$ to ensure support in $\mathcal{E}$ and then normalized to have mass 1.

Initial conditions will be discrete Maxwellians centered at $(x_{\text{init}}, v_{\text{init}})$, with standard deviation σ_0, with discrete homogeneous Dirichlet inflow boundary conditions (30d) enforced, and then normalized to have mass 1.

4.1. Performance of the scheme

We present here some numerical tests aimed at assessing the performance of the proposed scheme (30) in comparison with standard schemes detailed in Appendix C. To make the experiment as meaningful as possible, the tests were conducted in a nonlinear regime (in the sense of N^k being non-negligible throughout the simulation), with the grid defined by $x_{\min} = -9$, $V = 25$, the initial datum centered at $(x_{\text{init}}, v_{\text{init}}) = (7, 15)$ with standard deviation $\sigma = 1$, the remaining parameters being $b = -10$, $\nu_{\text{ext}} = 0.1$, $\omega_0 = 1$, $\tau = 0.6$, $a_0 = a_1 = 1$, and $T = 1$ being the duration of the experiment.

Table 3 displays temporal refinement at fixed spatial-velocity steps, while Table 4 displays spatial-velocity refinement at fixed time step. The labels in the tables are to be understood as follows. The following columns contain a checkmark ✓ whenever the corresponding assertions are verified *throughout* the execution of the scheme, and a cross × otherwise:

- $V \gg 1$: Assumption (2) is satisfied,
- **CFL**: the CFL-type condition (35) is met,
- ≥ 0: the solution remains non-negative,
- **Mass**: the solution's mass remains equal to 1 up to a 10^{-10} tolerance,

The exact solution not being available, we also examine experimental orders of convergence (EOC) for the methods in $\alpha = \Delta t$ or $\alpha = h = \Delta x = \Delta v$. Let us denote by ϕ_α the final value (as in $f^{k_{\max}}$, for the set $\overline{\mathcal{K}}$ built for this Δt) of the numerical solution obtained by the scheme with α as a parameter. We introduce the following L^1 and L^∞ EOCs[4]:

$$\mathrm{O}_{\alpha,L^1} = \log_2 \frac{\mathscr{M}\left(\left|\phi_{4\alpha} - \phi_{2\alpha}\right|\right)}{\mathscr{M}\left(\left|\phi_{2\alpha} - \phi_{\alpha}\right|\right)}, \qquad \mathrm{O}_{\alpha,L^\infty} = \log_2 \frac{\max\limits_{\mathcal{E}_{\text{ext}}} \left|\phi_{4\alpha} - \phi_{2\alpha}\right|}{\max\limits_{\mathcal{E}_{\text{ext}}} \left|\phi_{2\alpha} - \phi_{\alpha}\right|}.$$

For the space-velocity EOCs, the factor two between successive grid sizes ensures that the coarser grid is embedded in the finer one. The finer-grid solution is therefore restricted to the coarser grid before computing the differences.

If at least one of the three runs needed to compute an EOC fails because non-finite values appear, the corresponding entry is marked as unstable. Runtime denotes the wall-clock execution time, measured in kiloseconds, needed to compute the approximate solution up to the final time T. All runtimes were measured on the same machine; "fail" indicates that the run failed.

First, scheme (30) appears to be the most robust method among the schemes tested in this nonlinear regime: it is the only one which simultaneously preserves non-negativity and mass throughout the simulations, while reaching the finest discretizations considered. These experiments are thus consistent with the discrete preservation of positivity and mass proved in Properties 3 and 4.

This robustness comes with an additional computational cost, especially in the coupled space-velocity refinement. However, the comparison shows that the extra cost is tied to the preservation of the qualitative structure: the alternative schemes are faster in some regimes but lose mass, positivity, or stability before reaching the finest refinements considered.

Moreover, the measured experimental orders of convergence approach 1 in the L^1 topology, both for temporal refinement Δt and for the coupled spatial-velocity refinement $h = \Delta x = \Delta v$.

The same qualitative conclusions were obtained in several additional experiments of the same type, not reported here, with different parameter choices and discretization ranges; this motivates the following conjecture:

Conjecture 1. The scheme (30) is first-order accurate in x, v, and t in the discrete L^1 topology for sufficiently smooth solutions of the regularized truncated problem (21).

[4]The definition of the extended grid $\mathcal{E}_{\text{ext}}$ is given in 1, the mass $\mathscr{M}$ on that grid being defined by (23).

Table 3
Satisfaction of previously introduced conditions, preservation of non-negativity, conservation of mass, EOC in L^1 and L^∞, and runtime for different temporal resolutions at fixed $h = 1/64$.

Scheme	Δt	$V \gg 1$	CFL	≥ 0	Mass	$O_{\Delta t, L^1}$	$O_{\Delta t, L^\infty}$	Runtime
Fully explicit centered	$10^{-2}/2^7$	×	×	×	×	unstable	unstable	fail
	$10^{-2}/2^8$	×	×	×	×	unstable	unstable	fail
	$10^{-2}/2^9$	✓	✓	×	×	unstable	unstable	6.5
	$10^{-2}/2^{10}$	✓	✓	×	×	unstable	unstable	13
Fully explicit upwind	$10^{-2}/2^7$	×	×	×	×	unstable	unstable	fail
	$10^{-2}/2^8$	×	×	×	×	unstable	unstable	fail
	$10^{-2}/2^9$	✓	✓	✓	×	unstable	unstable	8.8
	$10^{-2}/2^{10}$	✓	✓	✓	×	unstable	unstable	16
Semi-implicit centered	$10^{-2}/2^7$	✓	✓	×	×	unstable	unstable	2.0
	$10^{-2}/2^8$	✓	✓	×	×	1.008	1.016	3.9
	$10^{-2}/2^9$	✓	✓	×	×	1.004	1.008	7.7
	$10^{-2}/2^{10}$	✓	✓	×	×	1.002	1.004	13
Semi-implicit upwind (30)	$10^{-2}/2^7$	✓	✓	✓	✓	1.01	1.03	3.1
	$10^{-2}/2^8$	✓	✓	✓	✓	1.007	1.01	6.2
	$10^{-2}/2^9$	✓	✓	✓	✓	1.003	1.008	11
	$10^{-2}/2^{10}$	✓	✓	✓	✓	1.002	1.004	13

Table 4
Satisfaction of previously introduced conditions, preservation of non-negativity, conservation of mass, EOC in L^1 and L^∞, and runtime for different spatial resolutions at fixed $\Delta t = 10^{-5}$.

Scheme	h	$V \gg 1$	CFL	≥ 0	Mass	O_{h, L^1}	O_{h, L^∞}	Runtime
Fully explicit centered	2^{-6}	✓	✓	×	×	0.053	−0.002	29
	2^{-7}	×	×	×	×	unstable	unstable	fail
	2^{-8}	×	×	×	×	unstable	unstable	fail
	2^{-9}	×	×	×	×	unstable	unstable	fail
Fully explicit upwind	2^{-6}	✓	✓	✓	×	0.823	0.549	36
	2^{-7}	×	×	×	×	unstable	unstable	fail
	2^{-8}	×	×	×	×	unstable	unstable	fail
	2^{-9}	×	×	×	×	unstable	unstable	fail
Semi-implicit centered	2^{-6}	✓	✓	×	×	0.053	−0.002	9.1
	2^{-7}	✓	✓	×	×	0.026	−0.001	37
	2^{-8}	✓	✓	×	×	0.013	0.0007	172
	2^{-9}	×	×	×	×	unstable	unstable	fail
Semi-implicit upwind (30)	2^{-6}	✓	✓	✓	✓	0.823	0.549	14
	2^{-7}	✓	✓	✓	✓	0.897	−0.066	54
	2^{-8}	✓	✓	✓	✓	0.943	−0.006	338
	2^{-9}	✓	✓	✓	✓	0.969	0.038	2542

This conjecture is motivated by the observed discrete L^1 self-convergence and by a first-order consistency estimate in the weighted discrete L^1 norm established in the extended version [70, Section III.4.3]. A complete convergence proof is not pursued here, since the nonlinear dependence of the update on the discrete activity N^k makes the stability analysis substantially more delicate than in the linear Lax-Richtmyer setting. In particular, one would need to control the propagation of perturbations through the nonlinear coupling between N^k and f^k. The proof of Conjecture 1 therefore remains a challenging open problem.

The temporal refinement also gives a clean first-order-in-t behavior in the L^∞ topology; but by contrast to that temporal well-established behavior, the L^∞ EOC under spatial-velocity refinement is unstable and does not display a

clear asymptotic regime. We do not interpret that as a failure of the scheme: the reset mechanism is indeed prone to building solutions which might develop stiffness in (x, v) (as we cannot for example, by simple analysis of the original measure-right-hand-side equation which we approach here, have C^1_x and C^2_v regularity).

The L^1 topology is therefore more natural for the present model, both because the unknown is a probability density and because the main structural property is mass transport.

Remark 4.1. The experiments confirm that the CFL condition (35) is not sharp as non-negativity preservation can be achieved without it in some cases.

Remark 4.2. For technical reasons we took $\Delta x = \Delta v$ in all our experiments. Since the chosen discretization for the transport part forces order 1 in v at best, it was enough for our EOC study. But studies on the regularity of the solution should likely make a distinction Δx and Δv as the only "true" diffusion is in v for our operator, the apparent diffusion in x coming through the hypoelliptic cross transport-diffusion mechanism mentioned earlier.

4.2. Mean-field comparison with Brian 2 simulations

Theoretical as well as experimental considerations indicated that scheme (30) was a good candidate to obtain numerical approximations of solutions to the continuous bounded Problem (21), which simplifies (18) while retaining the same physical constraints on its solutions. We now aim at comparing the behavior of solutions obtained via scheme (30) with the mean behavior of a population of RF neurons having compatible parameters. This comparison follows the same rationale as in [13]: the goal is not to prove a mean-field limit, but to test whether the kinetic description captures the main observables of the underlying particle system.

We use the neuron and synapse simulator Brian 2 [62] already used earlier in this work for single neuron simulations. The Brian 2 population contains a large number of M RF neurons split into M_E neurons with excitatory outgoing synapses and M_I with inhibitory outgoing synapses. In order to limit the influence of the finite-size model stochasticity, we performed $Q > 1$ independent runs.

All parameter values used in the comparisons of this subsection are collected in Table D.1.

We compare the two descriptions through three observables: the mean voltage $X(t)$, the final voltage density $\rho(x, T)$, and the activity $N(t)$.

The Brian 2 initial states are sampled from the same Gaussian density as the PDE initial datum, conditioned to lie inside the truncated computational domain. The mean voltage is computed as the empirical average of the particle voltages, while the final voltage density is obtained by histogramming the particle voltages at time T on the PDE x-grid. The Brian 2 activity is computed from spike counts in bins of width Δt_{bin}, divided by the population size and by the bin width.[5]

4.2.1. Graphical comparison

The PDE observables are computed from the numerical density by discrete quadrature, with $X(t)$ given by the first x-moment, $\rho(x, T)$ by integration in v, and $N(t)$ by the discrete boundary-flux formula used in the scheme.

For each Brian 2 observable, we plot the mean over all the Q runs, as well as one standard deviation around it.

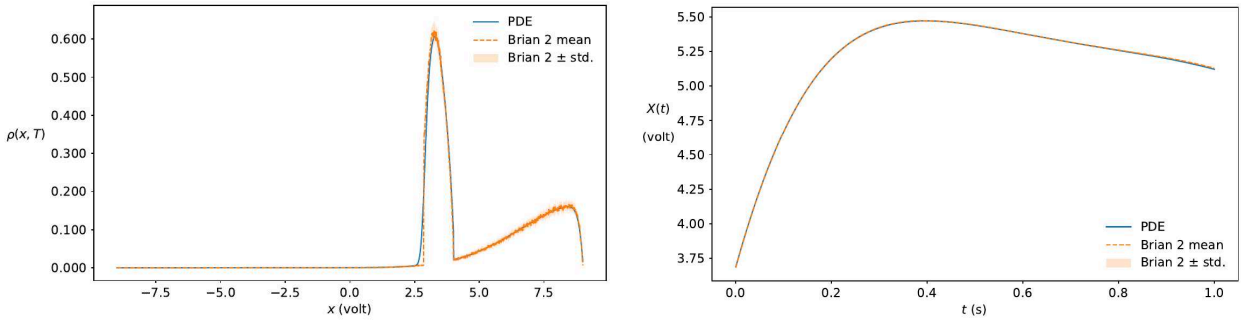


Figure 8: Comparison between the PDE solution computed with scheme (30) and finite-size Brian 2 simulations for the final voltage density (left) and the mean voltage (right).

[5] Changing the bin width modifies the short-time fluctuations of the Brian 2 activity but does not change the qualitative comparison reported below.

Figure 8 shows good agreement for the state observables in this parameter regime. The PDE mean voltage closely follows the empirical Brian 2 mean throughout the simulation. The final voltage density is also well captured, with only a small mismatch near $x \simeq 2.5$, where the finite-size histogram remains slightly rough.

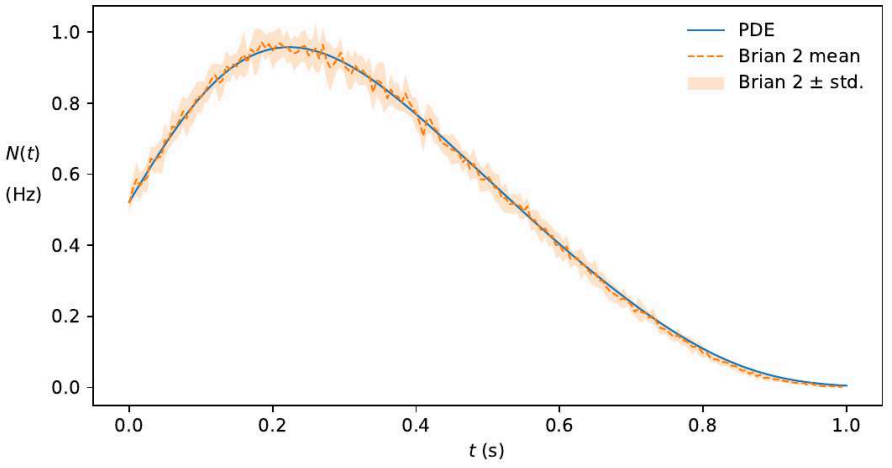


Figure 9: Comparison between the PDE activity and the activity obtained from finite-size Brian 2 simulations.

The activity comparison in Figure 9 is more delicate, since $N(t)$ is obtained from binned spike counts in the particle system and from a discrete boundary-flux formula in the PDE. The short-time discrepancy is therefore not unexpected. Nevertheless, the PDE activity remains within one standard deviation of the Brian 2 mean and captures the mid-time behavior accurately.

These results support the relevance of the kinetic description in this parameter regime. They also provide combined numerical evidence for the adequacy of the regularized truncated problem (21) and of the scheme (30), since the kinetic model is observed through its discretization.

In the following experiments, we isolate several parameters and vary them one at a time, while keeping all other parameters fixed. Besides assessing the sensitivity of the PDE-Brian 2 comparison to these parameters, these tests also examine the robustness of the agreement across several parameter choices.

Our key observables are L^2 differences in mean voltage and activity between the PDE simulated via scheme (30), and the mean value of the Brian 2 simulations. The L^2 difference for X, denoted $L^2_X := \left\| X_{\text{Brian 2}} - X_{\text{PDE}} \right\|_{L^2(0,T)}$, is computed directly from the values of $X_{\text{Brian 2}}$ and X_{PDE} at the common time nodes t_k, for $k \in \overline{\mathcal{K}}$, using the trapezoidal rule in time. For the L^2 difference for N, denoted $L^2_N := \left\| N_{\text{Brian 2}} - N_{\text{PDE}} \right\|_{L^2(0,T)}$, the Brian 2 activity is linearly interpolated onto the PDE time grid before applying the same trapezoidal rule.

4.2.2. Influence of time and mesh refinement

As shown in Table 5, refining the time step does not reduce the L^2 difference between the PDE and Brian 2 mean-voltage curves in this regime. Since the largest value of Δt considered here is already close to the largest empirically admissible value for which the scheme retains its structure-preserving behavior, the observed saturation suggests that the time-discretization error is dominated by other sources in this regime.

By contrast, refining the spatial-velocity mesh has a visible effect. This is consistent with the expected sensitivity of the comparison to Δx, since Δx enters the boundary-flux discretization used to compute $(N^k)_k$, notably through the horizontal trace formula (34), and also affects voltage-related observables.

4.2.3. Influence of kick size and left truncation of the computational domain

Table 6 shows that the difference decreases as the kick size is reduced from $K = 10^{-3}$ to $K = 10^{-5}$, before reaching a saturation level. This is consistent with the small-kick assumption used in the diffusion approximation underlying the derivation of the kinetic model in Section A.

In the same regime, the left truncation $x_{\min}$ has essentially no influence on the observed L^2 difference. This is expected from the location and direction of the dynamics, since the deterministic v-drift is centered around

Table 5
Influence of the time step and mesh size on the mean-voltage difference. Left: time-step refinement with fixed $\Delta x = \Delta v = 1/21$. Right: mesh refinement with fixed $\Delta t = 10^{-5}$.

Time-step refinement	
Δt	L_X^2
5×10^{-4}	1.2536×10^{-2}
10^{-4}	1.2738×10^{-2}
5×10^{-5}	1.2765×10^{-2}
10^{-5}	1.2787×10^{-2}
5×10^{-6}	1.2790×10^{-2}

Mesh refinement	
$\Delta x = \Delta v$	L_X^2
1/16	1.6632×10^{-2}
1/21	1.2793×10^{-2}
1/26	1.0403×10^{-2}
1/31	8.7720×10^{-3}
1/36	7.5890×10^{-3}
1/46	5.9870×10^{-3}
1/51	5.4210×10^{-3}

$x = bv_{\text{ext}}/\omega_0^2$. The initial condition $(x_{\text{init}}, v_{\text{init}}) = (4, 15)$ lying in the upper half-plane, the final time $T = 1$ being short, and the value $bv_{\text{ext}}/\omega_0^2 = 6 \times 10^{-5}$ therefore imply that the density is not significantly transported toward the artificial left boundary before firing occurs.

Table 6
Influence of the kick size and left truncation on the mean-voltage difference. Left: dependence on the kick size $K = J/(C\tau_{\text{syn}})$ for fixed truncation $x_{\min} = -36$. Right: dependence on the left truncation $x_{\min}$ for fixed kick size $K = 10^{-6}$.

Kick-size sensitivity	
K	L_X^2
10^{-3}	1.6608×10^{-2}
10^{-4}	1.6345×10^{-2}
10^{-5}	1.6070×10^{-2}
10^{-6}	1.6100×10^{-2}

Left-truncation sensitivity	
$x_{\min}$	L_X^2
−21	1.6100×10^{-2}
−26	1.6100×10^{-2}
−31	1.6100×10^{-2}
−36	1.6100×10^{-2}

The situation changes in a regime where the drift favors transport toward the left boundary. This is illustrated in Table 7, for an initial condition $(x_{\text{init}}, v_{\text{init}}) = (2, -15)$, a final time $T = 10$ and $bv_{\text{ext}}/\omega_0^2 = -6$. Since the effective center of the deterministic drift lies far to the left of the initial position, while the initial velocity is already negative, over this longer time interval, the density is carried toward decreasing values of x, to the point of making the computations sensitive to the position of the left boundary.

The L^2 difference for X drops sharply as $x_{\min}$ is moved away from the region reached by the density, before saturating once the artificial left boundary is sufficiently far. The same behavior is observed for the activity N, but with a much stronger dependence on $x_{\min}$. When $x_{\min}$ is too close to the evolving density, all mass leaving through the artificial left boundary contributes, through the definition of N^k in scheme 30, to the reset source near $(u_{\text{R}}, 0)$. This produces an artificial reset mechanism, visible in Figure 10, which is absent from both the single-neuron model and the original Problem (18). The numerical results therefore illustrate the importance of placing the artificial left boundary sufficiently far to the left.

Table 7
Influence of the left truncation $x_{\min}$ in a left-transport regime. The table reports the $L^2(0,T)$ norms of the differences between the PDE solver and the particle simulation for the activity $N(t)$ and the mean voltage $X(t)$.

$x_{\min}$	L_N^2	L_X^2
−7	9.5526×10^{-1}	1.1801×10^{1}
−9	1.0464×10^{-1}	1.2639
−11	1.5665×10^{-4}	1.0749×10^{-1}
−13	5.1139×10^{-9}	1.0901×10^{-1}
−15	5.8930×10^{-15}	1.0901×10^{-1}

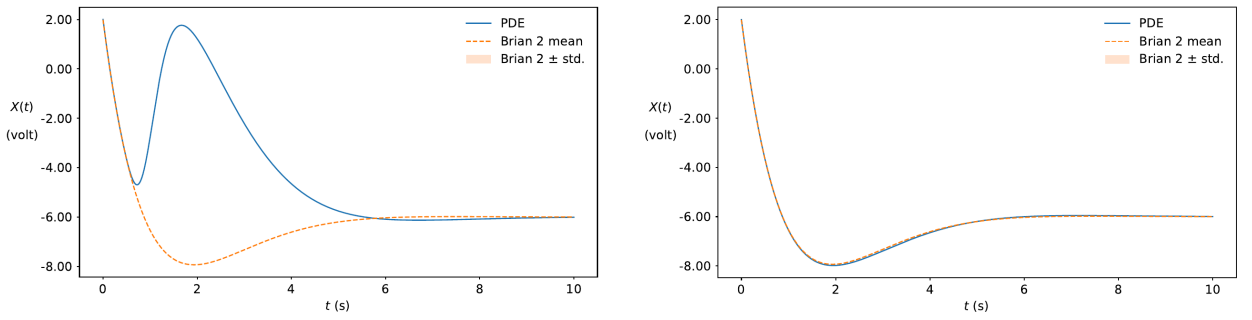


Figure 10: Mean voltage for $x_{\min} = -7$ (left), and $x_{\min} = -11$ (right).

4.2.4. Influence of the number of point neurons

Here for each value of the total number of particles M, the Brian 2 network consists of 80% excitatory neurons and 20% inhibitory neurons.

The results of Table 8 indicate that the L^2 difference remains of the same order for all tested values of M, but a slight overall improvement is observed as the number of particles increases; this is consistent with the work [13] in which the authors underlined the fact that good accuracy was already observed for relatively small values of M. The decrease is not strictly monotone, which is expected since the Brian reference is itself an empirical average over finitely many stochastic realizations. The smallest difference is obtained for the largest network size $M = 10^5$, consistently with the interpretation of the kinetic equation as a mean-field approximation of the particle system.

Table 8
Influence of the number of point neurons in the Brian 2 simulations.

M	M_E	M_I	L^2_X
10^3	800	200	1.5903×10^{-2}
5×10^3	4000	1000	1.3470×10^{-2}
10^4	8000	2000	1.4482×10^{-2}
5×10^4	40000	10000	1.3583×10^{-2}
10^5	80000	20000	1.2687×10^{-2}

4.3. Numerical investigation of representative regimes

We now use scheme (30) to illustrate several qualitative dynamical regimes of the nonlinear RF equation. The purpose is not to give an exhaustive parameter study, but to show that the scheme captures several mechanisms suggested by the model: reset-driven transients, subthreshold damped oscillations, low-activity transport far from the threshold, and feedback-driven oscillations. The parameters are listed in Table D.2; 2D and 3D videos displaying the evolution of numerical solutions in the studied regimes are available on YouTube and PeerTube.

Before comparing the observables associated with these regimes, it is useful to display one representative density evolution in phase space. Figure 11 corresponds to a reset-driven regime and illustrates three key features of the model: the reinjection of mass at the reset point $(u_R, 0)$ after threshold crossing, the spiral-like transport induced by the drift, and the spreading of the density in both variables through the hypoelliptic transport-diffusion mechanism.

The four regimes are then compared through macroscopic observables. Figures 12 and 13 display the mean voltage and activity for the representative experiments.

The first experiment corresponds to the reset-driven regime illustrated in Figure 11, obtained from an initial density placed close to the firing threshold. The density is rapidly transported toward $x = u_F$, producing an activity burst and a visible reinjection of mass near $(u_R, 0)$ shown in the associated voltage drop. The mean voltage and the activity then decrease and stabilize after the main reset event.

The second experiment displays subthreshold damped oscillations at the population level. The mean voltage oscillates with decreasing amplitude, and the activity exhibits peaks when the transported density returns toward the

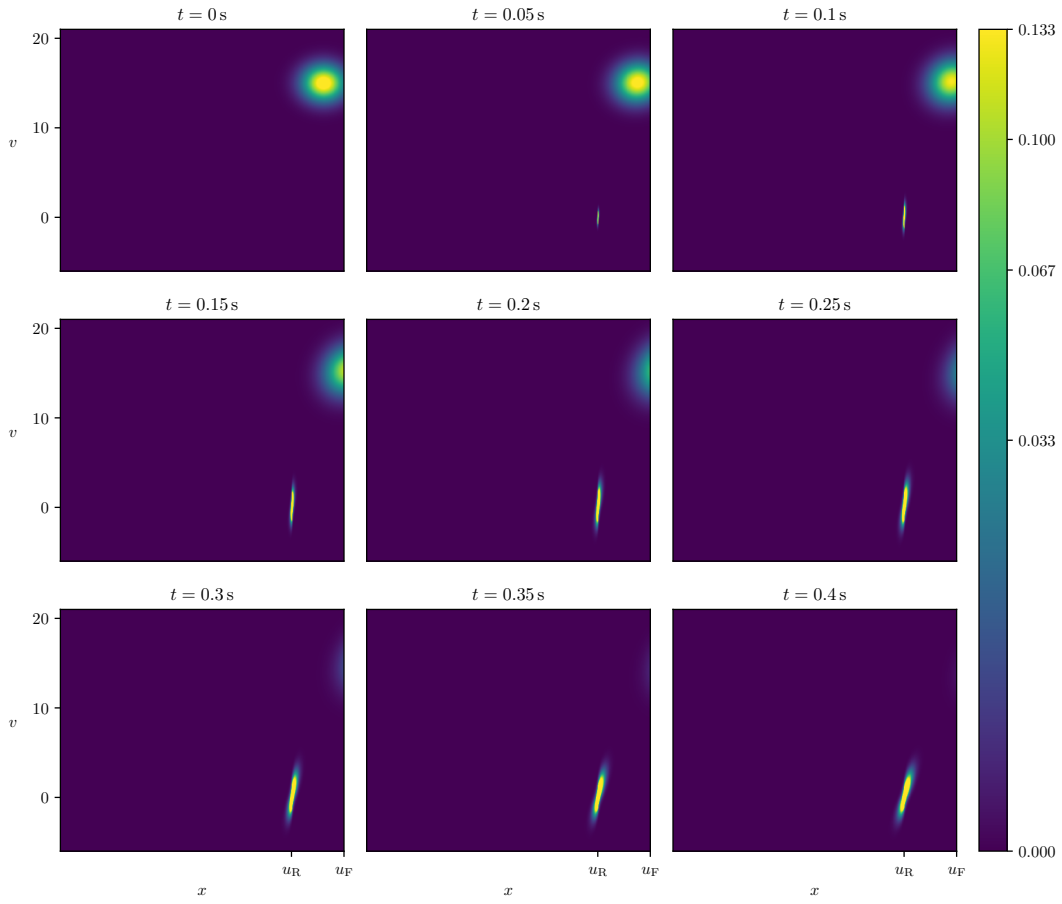


Figure 11: Snapshots of the numerical density in phase space in the reset-driven regime.

firing region. This shows that the resonator structure remains visible in the mean-field equation, even after averaging over the population.

The third experiment is initialized far from the firing threshold. In this case the activity remains extremely small, of order μHz, compared with values of order Hz in the other regimes; see Figure 13. The dynamics are dominated by transport, confinement and diffusion rather than by reset. The observed evolution is therefore close to the behavior suggested by the underlying linear drift-diffusion structure, with only a negligible contribution from the source term.

The last experiment is a feedback-driven oscillatory regime. Here the reset point is chosen closer to the firing threshold and the diffusion coefficients are very small, in order to isolate the transport-reset-feedback mechanism. The mean voltage and the activity display pronounced oscillations over the simulated time interval. Since no time-periodic forcing is imposed, these oscillations are generated by the internal coupling between transport, threshold crossing, reset, diffusion, and the activity-dependent drift. This provides numerical evidence that the nonlinear RF equation can generate long-lived feedback-driven oscillations at the population level.

It is worth emphasizing, however, that this last experiment is not the most extreme oscillatory regime encountered during the numerical exploration. In several parameter ranges, the activity grew much more rapidly. However these regimes were difficult to explore with the present scheme, for structural reasons. Indeed, Assumption (2) imposes

$$V > \tau \left(X\omega_0^2 + |b| \left(\nu_{\mathrm{ext}} + N^k \right) \right) + \Delta v.$$

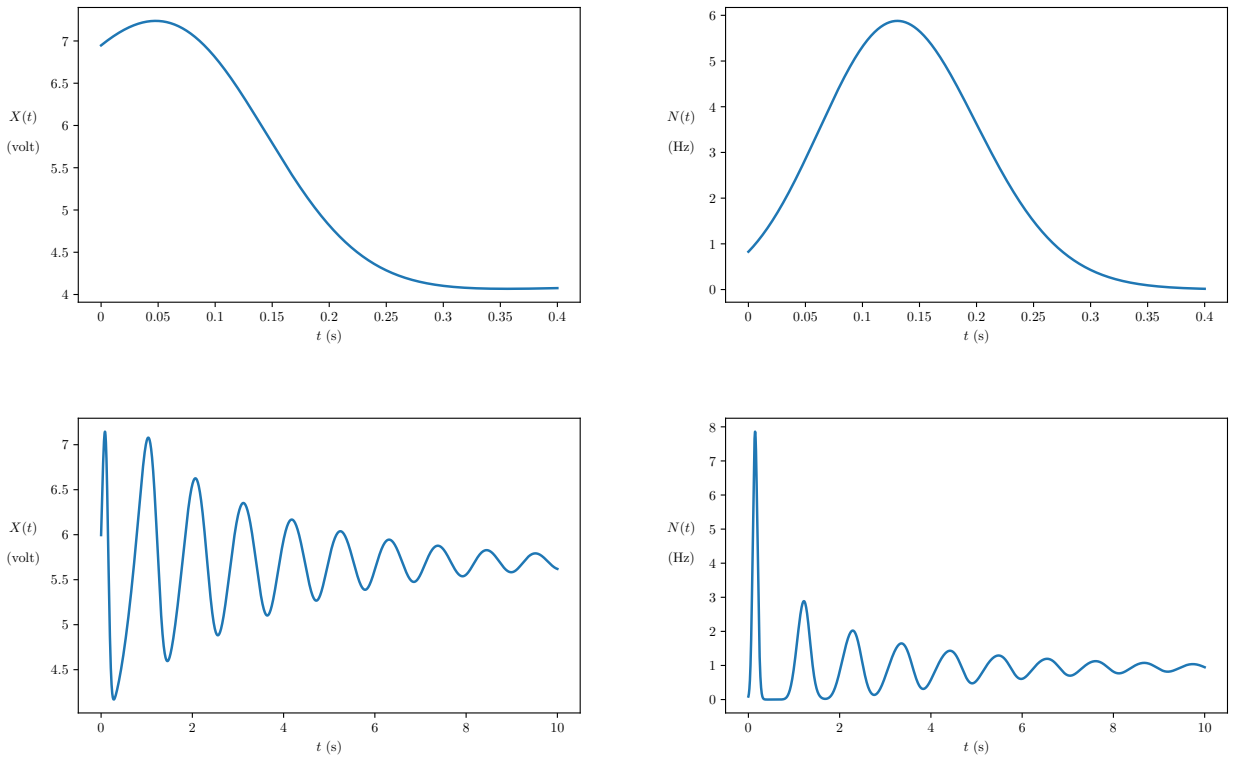


Figure 12: Mean voltage and activity in the reset-driven (top) and subthreshold damped oscillatory (bottom) regimes.

Thus, at fixed physical parameters, a growth of N^k forces the velocity domain to be enlarged if one wants to preserve the vertical confinement structure used in the proof of mass conservation. This substantially increases the number of velocity grid points and therefore the computational cost.

A similar restriction appears through the CFL condition: as N^k grows, the admissible time step Δt decreases. Hence the strongest feedback regimes are precisely those in which the present conservative scheme becomes the most demanding. This numerical obstruction should not be interpreted as a failure of the model, but rather as an indication that a more refined numerical strategy may be necessary to explore the strongest feedback regimes.

We therefore obtain numerical evidence of feedback-driven oscillations, but leave open the question of whether the continuous model admits activity growth as $t \to +\infty$. This question is closely related to the possible bifurcation structure of the equation and seems to be one of the most interesting directions opened by the present numerical experiments.

Remark 4.3. A natural extension would be to study the response to time-periodic external activity, in analogy with single-neuron resonance experiments such as [30]: instead of looking only for self-sustained oscillations, one could prescribe a time-periodic external activity $\nu_{\mathrm{ext}}(t)$, for instance a non-negative sinusoidal modulation, and study the population response as a function of the forcing frequency. This would provide a direct way to compare the frequency-selective behavior of the mean-field RF equation with the resonance properties observed at the single-neuron level. Since the coefficients of the matrices at play have to be recomputed at each step anyway, this modification would come at essentially no cost to each individual simulation.

Remark 4.4. We also monitored Shannon's entropy $S(t)$ and the Fisher information $I_{\mathrm{F}}(t)$ in the four regimes. These quantities did not indicate a monotonicity law, which is not surprising given the simultaneous presence of transport, degenerate diffusion, threshold loss, singular reinjection, and nonlinear activity feedback. They were nevertheless useful observables: in the regimes considered here, both quantities eventually became nearly constant over the

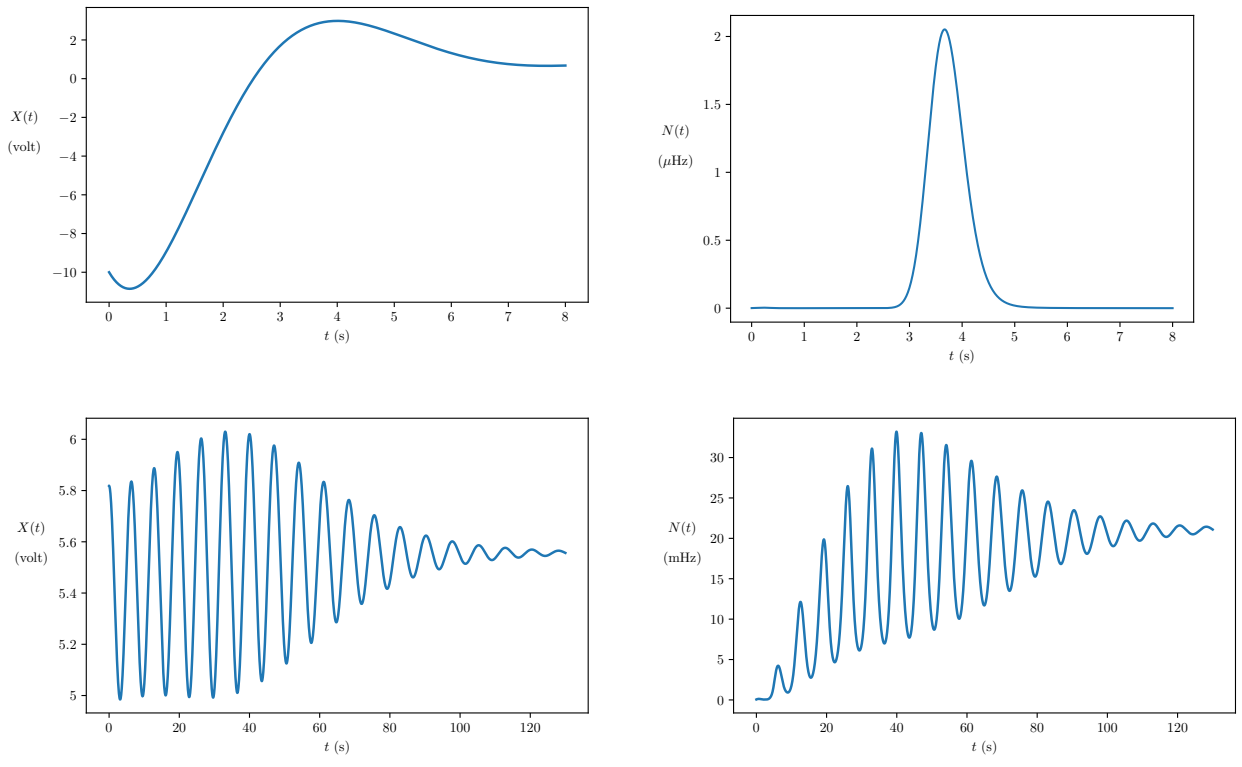


Figure 13: Mean voltage and activity in the far-from-threshold (top) and feedback-driven oscillatory (bottom) regimes.

simulated time interval. This observation suggests that the dynamics may approach long-time stable profiles, and motivates the more specific relative-entropy diagnostics considered below.

Remark 4.5. For practical reasons, we didn't choose the discretization parameters used in the first, second, and fourth regimes so that Assumption 2 is satisfied. The computed critical index is clipped to $[\![-j_{\max}, j_{\max}-1]\!]$, with the correction applied according to the local drift sign, and the velocity-boundary update formulas are retained even when the drift points outward. Consequently, Properties 3 and 4 do not provide an a priori guarantee for these runs. Nevertheless, the observed physical properties remained very satisfactory, which explains why we still presented the associated results.

4.4. Long-time behavior

4.4.1. Numerical long-time profiles

The previous experiments suggest that, for the parameter choices considered here, the transient dynamics eventually approach stable long-time profiles. To investigate this numerically, we extend the simulations to a final time T_∞ much larger than the time interval used in Subsection 4.3, and denote by f_∞ the numerical solution obtained at T_∞, the parameters still being listed in Table D.2. This notation is purely numerical: no existence or uniqueness result for stationary solutions is proved here.

Figure 14 displays the numerical long-time profiles in the four representative regimes as phase-space density plots. In the reset-driven regime, the profile is concentrated near the reset region and exhibits an elongated transport structure between the reset point and the firing boundary. This structure is also visible in the 3D representation shown in Figure 15. It reflects the combined effect of transport toward threshold, reinjection near $(u_R, 0)$, and hypoelliptic diffusion.

A similar transport-reset loop is visible in the subthreshold damped regime. In the far-from-threshold regime, the long-time profile is smoother and remains mostly away from the firing boundary, consistently with the very small activity observed in Figure 13 (upper-right panel). In the feedback-driven oscillatory regime, the profile still carries the imprint of the reset loop, as illustrated in Figure 15. On the longer time interval used here, the macroscopic oscillations eventually damp out for this parameter set.

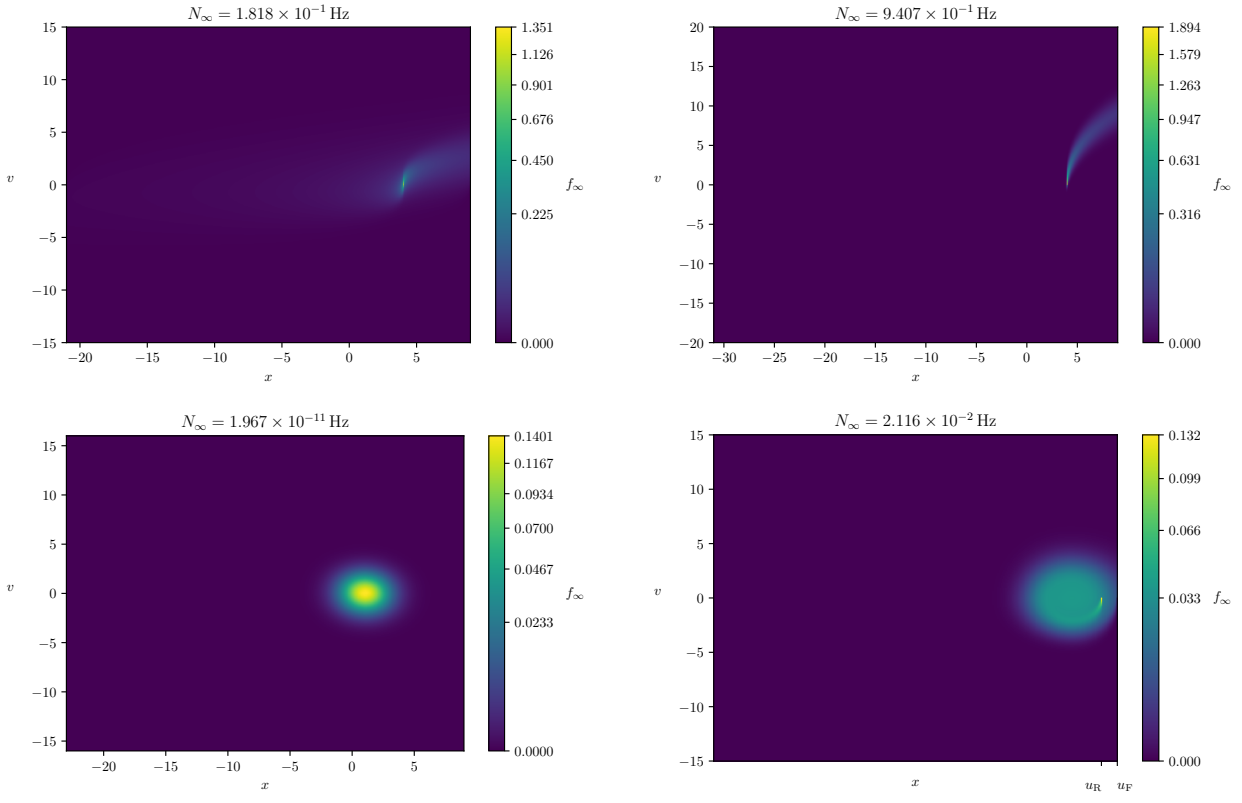


Figure 14: Numerical long-time profiles f_∞ obtained at time T_∞ in the four representative regimes as two-dimensional phase-space plots, from left to right and top to bottom: reset-driven, subthreshold damped oscillations, far-from-threshold, feedback-driven oscillations.

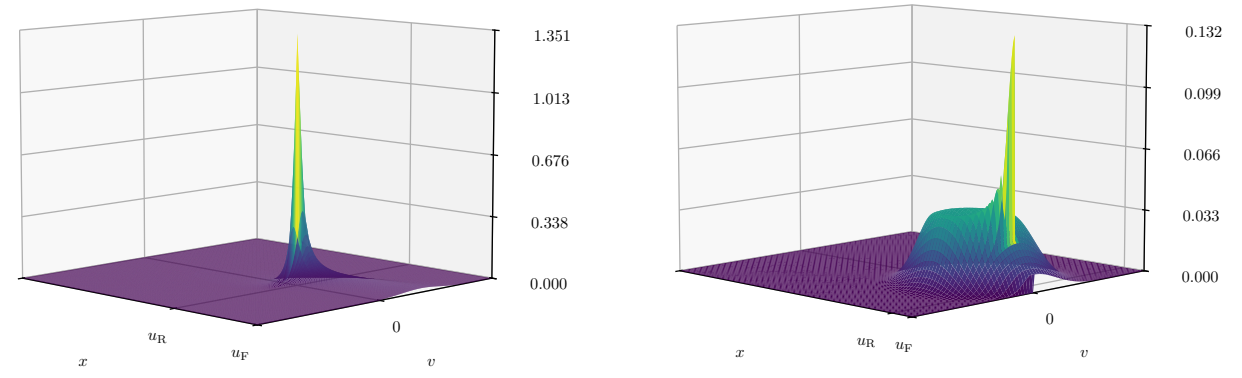


Figure 15: 3D numerical long-time profiles f_∞ obtained at time T_∞, from left to right: reset-driven regime, feedback-driven oscillations.

4.4.2. Relative entropy with respect to numerical long-time profiles

Entropy methods have been studied for Fokker-Planck equations arising in neuroscience, both from a theoretical perspective [15, 21] and from a numerical perspective [40]. In these works, the entropy is typically measured relative to a stationary profile.

For simplified integrate-and-fire Fokker-Planck models, relative entropy methods can be used to prove relaxation toward equilibrium under suitable assumptions. For instance, [21, Theorem 4.2] establishes monotonicity of a relative entropy functional for a linear one-dimensional model, under decay and domination assumptions.

Motivated by these results, we define a relative entropy by adapting the formula introduced in [21] to our geometry.[6] At the continuous level, this definition would require the existence of a positive stationary profile f_∞. In the computations below, however, f_∞ denotes the numerical long-time profile obtained at time T_∞. For $t \in (0, \infty)$:

$$\mathcal{H}_{\mathrm{rel}}(t) := \int_E f_\infty(x, v) \ln\left(\frac{f_\infty(x, v)}{f(x, v, t)}\right) \mathrm{d}x\, \mathrm{d}v. \tag{40}$$

The discrete entropy is evaluated by quadrature, discarding values of $f(x, v, t)$ or $f_\infty(x, v)$ below machine precision (see [70] for a discussion around this choice).

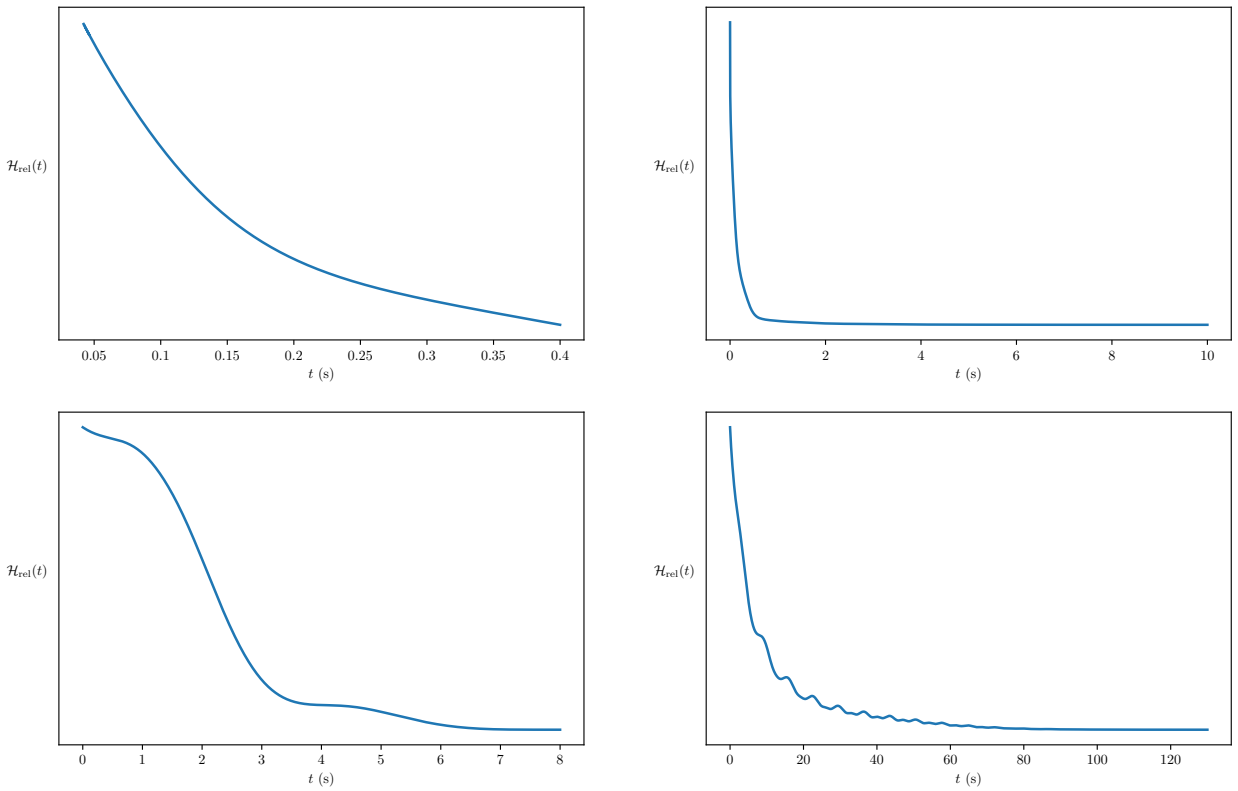


Figure 16: Logarithmic relative entropy $\mathcal{H}_{\mathrm{rel}}(t)$ with respect to the numerical long-time profile f_∞ in the four representative regimes, from left to right and top to bottom: reset-driven, subthreshold damped oscillations, far from threshold, feedback-driven oscillations.

The corresponding relative entropy curves are shown in Figure 16; the curves are plotted on the original time interval $[0, T]$ used in Subsection 4.3, while f_∞ is computed from the longer simulation up to T_∞.

In the first three regimes, the logarithmic relative entropy decreases toward zero, supporting the interpretation of relaxation toward a numerical steady profile. The feedback-driven oscillatory regime is more delicate: the solution first undergoes a large oscillatory transient before entering the apparent basin of attraction of the long-time profile. The corresponding relative quantities are therefore less regular at early times, but remain consistent with eventual relaxation.[7]

[6] In their terminology this corresponds to the convex choice $G(r) = -\ln r$ making $\mathcal{H}_{\mathrm{rel}}(t)$ indeed admissible as a relative entropy functional.

[7] It must be noted that in this very small diffusion regime, numerical diffusion may substantially influence the computed long-time profile; its interpretation in terms of the continuous dynamics therefore opens an interesting direction for investigation.

These computations suggest that stationary profiles may act as attractors for some parameter regimes of the RF mean-field equation. They cannot, however, be interpreted as an indication of entropy dissipation at the continuous level, as the feedback-driven oscillatory relative entropy does not display monotone decay in Figure 16.

Quadratic relative entropies have also been used to obtain exponential decay estimates for related models (see Theorem 2.1 in [15] and Theorem 1.2 in [27]). We tested such quantities in the present setting (see the long version [70]), but they did not reveal a clearer monotonicity pattern in the feedback-driven regime.

The scheme (30) was designed to preserve mass and non-negativity, but not to enforce a discrete entropy inequality. Thus, any lack of monotonicity observed in the relative quantities may reflect either the continuous dynamics or the numerical discretization. A theoretical study of steady states and entropy dissipation remains open, and may lead to the creation of schemes better suited to the long-time structure of the equation.

5. Conclusion

The main outcome of this work is a kinetic mean-field framework for networks of noisy resonate-and-fire neurons, together with a numerical scheme adapted to its threshold-reset structure. The derived equation retains the genuinely two-dimensional phase-space geometry of the RF model, while incorporating the nonlinear feedback of the population activity through the drift, the diffusion coefficient, and the reset source. To the best of our knowledge, this provides the first tractable PDE framework in which population-level RF dynamics can be studied beyond direct finite-size simulations.

On the numerical side, the finite-difference scheme introduced here was designed to preserve the two most basic structural constraints of the model: conservation of total mass and preservation of non-negativity of the density. These properties were proved under explicit assumptions, and the numerical tests showed that these structural properties are important in practice. In particular, the comparison with more direct discretizations confirmed that preserving the structure of the equation is important in nonlinear threshold-reset regimes. In our experiments, small mass errors, most often in the form of mass gain, were amplified by the activity feedback and could rapidly corrupt the computation, often together with loss of positivity or unstable activity estimates.

The comparison with finite-size Brian 2 simulations gave good agreement for the mean voltage, the final voltage density, and the population activity. Further simulations displayed several qualitative regimes: reset-driven transients, subthreshold damped oscillations, low-activity far-from-threshold dynamics, and feedback-driven oscillatory transients. These regimes illustrate the combined influence of transport, degenerate diffusion, threshold loss, reinjection, and nonlinear activity feedback in the RF mean-field equation.

The experiments also point to several open mathematical questions. A first one is the well-posedness of the continuous equation. The problem combines an unbounded kinetic domain, non-standard boundary traces, nonlinear activity-dependent coefficients, and a singular reset source. Once such a theory is available, the next natural question concerns the long-time behavior of solutions. The computations suggest relaxation toward numerical long-time profiles in several regimes, but also show that large oscillatory transients may occur. This raises the question of existence and stability of stationary states, and of whether relative entropy or Fisher-type quantities can be used to describe convergence toward them, at least for suitable initial data.

The numerical evidence further suggests that a bifurcation picture may underlie the transition between the regimes observed here. The literature on nonlinear noisy integrate-and-fire equations provides useful reference points, in particular concerning steady states, periodic solutions, delay effects, and activity blow-up phenomena [15, 16, 20–23, 28, 43, 58]. Related recent works have also used Doeblin-Harris techniques to obtain convergence and stability properties for more intricate models with partial diffusion [4, 61]. However, these results should not be expected to transfer directly. The RF equation has a different phase-space geometry and a different transport-diffusion mechanism. In particular, the large activity regimes observed numerically seem related to the firing-reset-feedback loop, rather than to the same finite-time blow-up mechanism as in the NNLIF equation.

Several numerical questions also remain open. The observed first-order behavior should be turned into a rigorous convergence result, which would require a stability mechanism adapted to the nonlinear activity, the reset source, and the boundary fluxes. It would then be natural to ask whether higher-order or finite-volume variants can be constructed while preserving non-negativity and conserving mass. Higher-order WENO-type discretizations, used for instance in the NNLIF literature to control spurious oscillations near sharp activity dynamics [21, 24], provide a natural reference point for future improvements. In the present setting, however, such an extension would have to be reconciled with the

structural constraints emphasized in this work. Another important direction would be to treat the Dirac delta directly, rather than through a smooth approximation.

A second numerical challenge concerns parameter regimes with large activity or realistic physiological constants. In such cases, the velocity domain required by the present conservative scheme can become very large, and the CFL restriction can become severe. Adaptive velocity grids, adaptive time stepping, or asymptotic-preserving methods [46, 47] may therefore be needed to explore these regimes efficiently. Such methods could also be useful for studying the strongest feedback-driven oscillatory regimes, where the current scheme becomes computationally demanding.

At the modeling level, a natural extension would be to relax the matching condition $\tau_{\text{syn}} = L/R_L$ used in the derivation of the population equation, for instance by retaining the synaptic current as an additional state variable. Such an extended formulation would provide a setting for investigating general synaptic time scales and assessing the accuracy of the present kinetic model when the two time constants are close.

We also note that the framework developed here may be useful beyond the particular RF network considered in this article. At an abstract level, the model couples kinetic transport, loss through a distinguished boundary, and nonlinear reinjection at a reset location. Similar transport-reinjection mechanisms may appear in other systems involving thresholds, saturation, renewal, or failure-and-restart dynamics. For instance, one may think of traffic or communication-network models in which agents are removed from one state after reaching a maximal admissible threshold and are then reinjected into the system.

Finally, recent works have introduced generalizations of the RF model [38], while other contributions have used RF-type mechanisms in hardware-oriented implementations based on magnetic skyrmions [6], in neuromorphic computing [1], and in deep learning [41]. This renewed interest is consistent with the fact that the RF neuron combines rich dynamical behavior with a relatively simple computational structure. A deeper mathematical and numerical understanding of this model may therefore support further developments, both in mathematical neuroscience and in related computational applications.

A. Derivation of the Fokker-Planck equation

From expression (8), we have:

$$S(t) = \left(\frac{R_L}{LC} - \frac{1}{C\tau_{\text{syn}}}\right) I(t) + \frac{J_{\text{E}}}{C\tau_{\text{syn}}} \sum_{i=1}^{c_{\text{E}}} \sum_{j\in\mathbb{N}} \delta(t - t^i_{\text{E}_j}) - \frac{J_{\text{I}}}{C\tau_{\text{syn}}} \sum_{i=1}^{c_{\text{I}}} \sum_{j\in\mathbb{N}} \delta(t - t^i_{\text{I}_j}).$$

In order to obtain a closed two-dimensional description in the variables (x, v), we impose the simplifying assumption

$$\tau_{\text{syn}} = L/R_L,$$

which makes the first term on the right-hand side disappear.

Then for any time $t \in \mathbb{R}$:

$$S(t) = \frac{J_{\text{E}}}{C\tau_{\text{syn}}} \sum_{i=1}^{c_{\text{E}}} \sum_{j\in\mathbb{N}} \delta(t - t^i_{\text{E}_j}) - \frac{J_{\text{I}}}{C\tau_{\text{syn}}} \sum_{i=1}^{c_{\text{I}}} \sum_{j\in\mathbb{N}} \delta(t - t^i_{\text{I}_j}).$$

We now present a derivation inspired by those of [10, 13]. Let us assume, for the clarity of exposition, that we have a coupled network of *n purely excitatory* neurons (in the context of the EC layer II for example, stellate or pyramidal cells), with the evolutions of their membrane potentials governed by the equations and postulates of Section 2.2.

We can first notice that the pre-synaptic intensity arriving at the i-th neuron of the network can come either from a stimulus internal to the network or external, thus getting

$$I_i^{\text{pre}}(t) = \sum_{k=1}^{c_{\text{E}}^{\text{ext}}} \sum_j J_{ik}^{\text{ext}} \delta(t - t_j^{k,\text{ext}}) + \sum_{k=1}^{c_{\text{E}}^{\text{int}}} \sum_j J_{ik}^{\text{int}} \delta(t - t_j^k). \tag{A.1}$$

In equation (A.1), $c_{\text{E}}^{\text{ext}}, c_{\text{E}}^{\text{int}}$ is respectively the number of (excitatory) neurons exterior and interior to the network which are connected to neuron i, those numbers being considered constant throughout the network (thus independent of i) for simplification in writing. J_{ij}^{ext} and J_{ik}^{int} are the corresponding strengths of synaptic interconnections; $t_j^{k,\text{ext}}$ denotes

the j-th spike time of the k-th external excitatory source connected to neuron i, while t_j^k denotes the j-th spike time of the internal neuron k. For this calculation, we take homogeneous synaptic strengths $J_{ik}^{\text{int}} = J$ and $J_{ik}^{\text{ext}} = \omega$. The following expansion concerns the subthreshold dynamics; threshold loss and reinjection are accounted for separately.

The probability density function f associated with the probability of finding a typical neuron in the population with voltage in $(x, x + \mathrm{d}x)$ and voltage-velocity in $(v, v + \mathrm{d}v)$ at time t is given by:

$$f(x, v, t) = \mathbb{E}\left[\frac{1}{n}\sum_{i=1}^{n} \delta(x - X_i(t))\delta(v - V_i(t))\right], \tag{A.2}$$

where $(X_i(t), V_i(t))$ corresponds to the couple membrane potential/velocity at time t of the i-th neuron in the network of size n.

Let us denote, for Δt small,

$$E_i(x, v, t, \Delta t) := \mathbb{E}\left[\delta(x - X_i(t + \Delta t))\delta(v - V_i(t + \Delta t))\right] \tag{A.3}$$

and

$$e_i(x, v, t, \Delta t) := \mathbb{E}\left[\delta(x - X_i(t + \Delta t))\delta(v - V_i(t + \Delta t))|(X_i(t), V_i(t))\right]. \tag{A.4}$$

First, one can write, by considering the three possibilities in the interval $(t, t + \Delta t)$ which are

- no spike received,
- spike from exterior at time $t_{\text{ext}}^i \in (t, t + \Delta t)$,
- internal spike at time $t_{\text{int}}^i \in (t, t + \Delta t)$,

the following formula, up to $\mathcal{O}(\Delta t^2)$:

$$\begin{aligned} e_i(x, v, t, \Delta t) = &\left(1 - c_{\text{E}}^{\text{int}} N(t)\Delta t\right)\left(1 - c_{\text{E}}^{\text{ext}} \nu_{\text{ext}}(t)\Delta t\right)\delta\left(x - \left[X_i(t) + V_i(t)\Delta t\right]\right) \\ &\qquad \delta\left(v - \left[V_i(t) + \left(-\frac{V_i(t)}{\tau} - X_i(t)\omega_0^2\right)\Delta t\right]\right) \\ &+ c_{\text{E}}^{\text{int}} N(t)\Delta t\,\delta\left(x - X_i(t)\right)\delta\left(v - \left[V_i(t) + \frac{J}{C\tau_{\text{syn}}}\right]\right) \\ &+ c_{\text{E}}^{\text{ext}} \nu_{\text{ext}}(t)\Delta t\,\delta\left(x - X_i(t)\right)\delta\left(v - \left[V_i(t) + \frac{\omega}{C\tau_{\text{syn}}}\right]\right). \end{aligned}$$

Using formal Taylor expansions in x and v, understood in the sense of distributions, we retain terms to first order in Δt and to second order in the velocity-kick amplitudes $J/(C\tau_{\text{syn}})$ and $\omega/(C\tau_{\text{syn}})$. Denoting $d_i(x, v, t) := \delta(x - X_i(t))\delta(v - V_i(t))$, we obtain

$$\begin{aligned} e_i(x, v, t, \Delta t) =&(1 - c_{\text{E}}^{\text{int}} N(t)\Delta t)(1 - c_{\text{E}}^{\text{ext}} \nu_{\text{ext}}(t)\Delta t)\left(\delta(x - X_i(t))\,\delta\left(v - V_i(t) - \left(-\frac{V_i(t)}{\tau} - X_i(t)\omega_0^2\right)\Delta t\right)\right. \\ &\qquad \left. -V_i(t)\Delta t\,\frac{\partial}{\partial x} d_i(x, v, t)\right) \\ &+ c_{\text{E}}^{\text{int}} N(t)\Delta t\left(d_i(x, v, t) - \frac{J}{C\tau_{\text{syn}}}\frac{\partial}{\partial v} d_i(x, v, t) + \frac{J^2}{2C^2\tau_{\text{syn}}^2}\frac{\partial^2}{\partial v^2} d_i(x, v, t)\right) \\ &+ c_{\text{E}}^{\text{ext}} \nu_{\text{ext}}(t)\Delta t\left(d_i(x, v, t) - \frac{\omega}{C\tau_{\text{syn}}}\frac{\partial}{\partial v} d_i(x, v, t) + \frac{\omega^2}{2C^2\tau_{\text{syn}}^2}\frac{\partial^2}{\partial v^2} d_i(x, v, t)\right) \\ =&(1 - c_{\text{E}}^{\text{int}} N(t)\Delta t)(1 - c_{\text{E}}^{\text{ext}} \nu_{\text{ext}}(t)\Delta t) \\ &\left(d_i(x, v, t) - \left(-\frac{V_i(t)}{\tau} - X_i(t)\omega_0^2\right)\Delta t\frac{\partial}{\partial v} d_i(x, v, t) - V_i(t)\Delta t\,\frac{\partial}{\partial x} d_i(x, v, t)\right) \end{aligned}$$

$$+ c_{\mathrm{E}}^{\mathrm{int}} N(t)\Delta t\left(d_i(x,v,t) - \frac{J}{C\tau_{\mathrm{syn}}}\frac{\partial}{\partial v}d_i(x,v,t) + \frac{J^2}{2C^2\tau_{\mathrm{syn}}^2}\frac{\partial^2}{\partial v^2}d_i(x,v,t)\right)$$
$$+ c_{\mathrm{E}}^{\mathrm{ext}} \nu_{\mathrm{ext}}(t)\Delta t\left(d_i(x,v,t) - \frac{\omega}{C\tau_{\mathrm{syn}}}\frac{\partial}{\partial v}d_i(x,v,t) + \frac{\omega^2}{2C^2\tau_{\mathrm{syn}}^2}\frac{\partial^2}{\partial v^2}d_i(x,v,t)\right).$$

Now assuming $c_{\mathrm{E}}^{\mathrm{int}} = c_{\mathrm{E}}^{\mathrm{ext}} =: c$ and $J = \omega$, as well as using the identity

$$a\delta(z-a) = z\delta(z-a),$$

one gets:

$$\begin{aligned} e_i(x,v,t,\Delta t) =& d_i(x,v,t) - \Delta t\frac{\partial}{\partial v}\left[\left(-\frac{V_i(t)}{\tau} - X_i(t)\omega_0^2\right)d_i(x,v,t)\right] - \Delta t\frac{\partial}{\partial x}V_i(t)d_i(x,v,t) \\ &+c(\nu_{\mathrm{ext}}(t)+N(t))\Delta t\left(-\frac{J}{C\tau_{\mathrm{syn}}}\frac{\partial}{\partial v}d_i(x,v,t) + \frac{J^2}{2C^2\tau_{\mathrm{syn}}^2}\frac{\partial^2}{\partial v^2}d_i(x,v,t)\right) \\ =& d_i(x,v,t) - \Delta t\frac{\partial}{\partial v}\left[\left(\frac{cJ}{C\tau_{\mathrm{syn}}}\left(\nu_{\mathrm{ext}}(t)+N(t)\right) - \frac{v}{\tau} - x\omega_0^2\right)d_i(x,v,t)\right] \\ &-\Delta t\,\frac{\partial}{\partial x}\left[v d_i(x,v,t)\right] + \Delta t\frac{cJ^2}{2C^2\tau_{\mathrm{syn}}^2}\left(\nu_{\mathrm{ext}}(t)+N(t)\right)\frac{\partial^2}{\partial v^2}d_i(x,v,t). \end{aligned}$$

Using the following property of conditional expectation

$$\mathbb{E}\left[\delta(x - X_i(t+\Delta t))\delta(v - V_i(t+\Delta t))\right] = \mathbb{E}\left[\mathbb{E}\left[\delta(x - X_i(t+\Delta t))\delta(v - V_i(t+\Delta t)) \mid (X_i(t), V_i(t))\right]\right],$$

which can be rewritten in our context as

$$E_i(x,v,t,\Delta t) = \mathbb{E}\left[e_i(x,v,t,\Delta t)\right],$$

formula (A.2) as well as the linearity of the expectation, and finally taking the limit when Δt goes to 0 within the preceding second-order small-kick approximation, one gets equation (10), the inhibitory and external contributions being added by the same diffusion-approximation argument, with the corresponding signs in the drift and squared amplitudes in the diffusion coefficient.

B. Proof of the discrete upwind integration by parts lemma

Lemma 2 (Discrete upwind integration by parts)**.** Let f^k be in $\ell^1_+(\mathcal{E}_{\mathrm{ext}})$, and let us suppose that Assumption (2) is verified. Then the following upwind discrete integration by parts formula holds:

$$\begin{aligned} &\sum_{i=1}^{i_{\mathrm{F}}-1}\sum_{j=1-j_{\max}}^{j_{\max}-1}\left[\left(\mu_2\right)_{i,j}^k\right]^+\left(D_v^- f^k\right)_{i,j} - \left[\left(\mu_2\right)_{i,j}^k\right]^-\left(D_v^+ f^k\right)_{i,j} \\ &\qquad = \frac{1}{\tau}\sum_{i=1}^{i_{\mathrm{F}}-1}\sum_{j=1-j_{\max}}^{j_{\max}-1} f_{i,j}^k - \frac{1}{\Delta v}\sum_{i=1}^{i_{\mathrm{F}}-1}\left[e_i^k + \left[\left(\mu_2\right)_{i,1-j_{\max}}^k\right]^+ f_{i,-j_{\max}}^k \right. \\ &\qquad\qquad \left. + \left[\left(\mu_2\right)_{i,j_{\max}-1}^k\right]^- f_{i,j_{\max}}^k\right], \end{aligned} \tag{B.1}$$

where, for all $(i,k) \in \mathcal{I}\times\mathcal{K}$, $j_{\mathrm{c}}(i,k)$ is defined as in (24) and e_i^k as in (26).

Proof. At fixed $k \in \mathcal{K}$:

$$\sum_{i=1}^{i_{\mathrm{F}}-1}\sum_{j=1-j_{\max}}^{j_{\max}-1}\left[\left(\mu_2\right)_{i,j}^k\right]^+\left(f_{i,j}^k - f_{i,j-1}^k\right) - \left[\left(\mu_2\right)_{i,j}^k\right]^-\left(f_{i,j+1}^k - f_{i,j}^k\right)$$

$$
\begin{aligned}
&= \sum_{i=1}^{i_{\mathrm{F}}-1} \left(\sum_{j=1-j_{\max}}^{j_{\max}-1} \left[\left(\mu_2\right)_{i,j}^k \right]^+ f_{i,j}^k - \sum_{j=-j_{\max}}^{j_{\max}-2} \left[\left(\mu_2\right)_{i,j+1}^k \right]^+ f_{i,j}^k \right. \\
&\qquad \left. - \sum_{j=2-j_{\max}}^{j_{\max}} \left[\left(\mu_2\right)_{i,j-1}^k \right]^- f_{i,j}^k + \sum_{j=1-j_{\max}}^{j_{\max}-1} \left[\left(\mu_2\right)_{i,j}^k \right]^- f_{i,j}^k \right) \\
&= \sum_{i=1}^{i_{\mathrm{F}}-1} \left[\sum_{j=1-j_{\max}}^{j_{\max}-1} f_{i,j}^k \left(\left[\left(\mu_2\right)_{i,j}^k \right]^+ - \left[\left(\mu_2\right)_{i,j+1}^k \right]^+ - \left[\left(\mu_2\right)_{i,j-1}^k \right]^- + \left[\left(\mu_2\right)_{i,j}^k \right]^- \right) \right. \\
&\qquad - \left[\left(\mu_2\right)_{i,1-j_{\max}}^k \right]^+ f_{i,-j_{\max}}^k + \left[\left(\mu_2\right)_{i,j_{\max}}^k \right]^+ f_{i,j_{\max}-1}^k \\
&\qquad \left. - \left[\left(\mu_2\right)_{i,j_{\max}-1}^k \right]^- f_{i,j_{\max}}^k + \left[\left(\mu_2\right)_{i,-j_{\max}}^k \right]^- f_{i,1-j_{\max}}^k \right] \\
&= \sum_{i=1}^{i_{\mathrm{F}}-1} \left[\sum_{j=1-j_{\max}}^{j_{\max}-1} f_{i,j}^k \left(\left[\left(\mu_2\right)_{i,j}^k \right]^+ - \left[\left(\mu_2\right)_{i,j+1}^k \right]^+ - \left[\left(\mu_2\right)_{i,j-1}^k \right]^- + \left[\left(\mu_2\right)_{i,j}^k \right]^- \right) \right. \\
&\qquad \left. - \left[\left(\mu_2\right)_{i,1-j_{\max}}^k \right]^+ f_{i,-j_{\max}}^k - \left[\left(\mu_2\right)_{i,j_{\max}-1}^k \right]^- f_{i,j_{\max}}^k \right],
\end{aligned}
$$

this last equality coming from the sign of μ_2^k on the top and bottom of the grid given by Assumption (2). We can remark that we always have, for any given $i \in \mathcal{I}$ and $j \in \mathcal{J}$:

$$\left(\mu_2\right)_{i,j+1}^k < \left(\mu_2\right)_{i,j}^k < \left(\mu_2\right)_{i,j-1}^k.$$

From there,

- If $\left(\mu_2\right)_{i,j+1}^k \geq 0$:

$$\left[\left(\mu_2\right)_{i,j}^k \right]^+ - \left[\left(\mu_2\right)_{i,j+1}^k \right]^+ - \left[\left(\mu_2\right)_{i,j-1}^k \right]^- + \left[\left(\mu_2\right)_{i,j}^k \right]^- = \left[\left(\mu_2\right)_{i,j}^k \right] - \left[\left(\mu_2\right)_{i,j+1}^k \right] = \frac{\Delta v}{\tau}.$$

- If $\left(\mu_2\right)_{i,j+1}^k \leq 0$ and $\left(\mu_2\right)_{i,j}^k \geq 0$:

$$\left[\left(\mu_2\right)_{i,j}^k \right]^+ - \left[\left(\mu_2\right)_{i,j+1}^k \right]^+ - \left[\left(\mu_2\right)_{i,j-1}^k \right]^- + \left[\left(\mu_2\right)_{i,j}^k \right]^- = \left[\left(\mu_2\right)_{i,j}^k \right]$$

- If $\left(\mu_2\right)_{i,j}^k \leq 0$ and $\left(\mu_2\right)_{i,j-1}^k \geq 0$:

$$\left[\left(\mu_2\right)_{i,j}^k \right]^+ - \left[\left(\mu_2\right)_{i,j+1}^k \right]^+ - \left[\left(\mu_2\right)_{i,j-1}^k \right]^- + \left[\left(\mu_2\right)_{i,j}^k \right]^- = - \left[\left(\mu_2\right)_{i,j}^k \right]$$

- If $\left(\mu_2\right)_{i,j-1}^k \leq 0$:

$$\left[\left(\mu_2\right)_{i,j}^k \right]^+ - \left[\left(\mu_2\right)_{i,j+1}^k \right]^+ - \left[\left(\mu_2\right)_{i,j-1}^k \right]^- + \left[\left(\mu_2\right)_{i,j}^k \right]^- = \left[\left(\mu_2\right)_{i,j-1}^k \right] - \left[\left(\mu_2\right)_{i,j}^k \right] = \frac{\Delta v}{\tau}.$$

Now noticing, thanks to (24), that $\left| \left(\mu_2\right)_{i,j_{\mathrm{c}}(i,k)+1}^k \right| \leq \frac{\Delta v}{\tau}$ and $\left| \left(\mu_2\right)_{i,j_{\mathrm{c}}(i,k)}^k \right| < \frac{\Delta v}{\tau}$, we can write:

$$
\begin{aligned}
&\sum_{i=1}^{i_{\mathrm{F}}-1} \sum_{j=1-j_{\max}}^{j_{\max}-1} \left[\left(\mu_2\right)_{i,j}^k \right]^+ \left(f_{i,j}^k - f_{i,j-1}^k \right) - \left[\left(\mu_2\right)_{i,j}^k \right]^- \left(f_{i,j+1}^k - f_{i,j}^k \right) \\
&\qquad = \sum_{i=1}^{i_{\mathrm{F}}-1} \left[\sum_{j=1-j_{\max}}^{j_{\max}-1} \Delta v \frac{f_{i,j}^k}{\tau} - e_i^k - \left[\left(\mu_2\right)_{i,1-j_{\max}}^k \right]^+ f_{i,-j_{\max}}^k - \left[\left(\mu_2\right)_{i,j_{\max}-1}^k \right]^- f_{i,j_{\max}}^k \right],
\end{aligned}
$$

the integration by parts formula coming after division by Δv. □

C. Other algorithms of interest

Definition 9. For comparison purposes, we define the centered discretizations of the in-space differentiation operator $\frac{\partial}{\partial x}$ by, for all (i,j) in $\mathcal{I}\times\mathcal{J}$,

$$(D_x^c F)_{i,j} := \frac{F_{i+1,j} - F_{i-1,j}}{2\Delta x}, \tag{C.1}$$

and of the in-velocity differentiation operator $\frac{\partial}{\partial v}$ by, for all (i,j) in $\mathcal{I}\times\mathcal{J}$,

$$(D_v^c F)_{i,j} := \frac{F_{i,j+1} - F_{i,j-1}}{2\Delta v}. \tag{C.2}$$

For $(i,j)\in\mathcal{E}_{\text{ext}}\setminus\mathcal{E}$, corresponding to the x-boundary of $\overline{\mathcal{E}}$, we take:

$$(D_x^c F)_{i,j} := (D_x F)_{i,j}.$$

The discrete Dirichlet condition (30d) as well as the horizontal trace formulas 34 are used in all three schemes. The schemes are defined as follows, for (i,j,k) in $\mathcal{E}_{\text{ext}}\times\mathcal{K}$:

Fully explicit upwind Euler method:

$$\begin{cases}
\textbf{Euler step:}\\
\dfrac{f_{i,j}^{k+1}-f_{i,j}^k}{\Delta t} + (\mu_1 D_x f^k)_{i,j}^k + (\mu_2 D_v f^k)_{i,j}^k - d_{i,j} f_{i,j}^k - (a_0+a_1 N^k)(D_v^2 f^k)_{i,j} = N^k \rho_{i,j}, & \text{(C.3a)}\\
\textbf{Boundary Robin conditions:}\\
-(\mu_2^k)_{i,j_{\max}-1}^- f_{i,j_{\max}}^k - (a_0+a_1 N^k)(D_v^+ f^k)_{i,j_{\max}-1} = 0,\\
(\mu_2^k)_{i,1-j_{\max}}^+ f_{i,-j_{\max}}^k - (a_0+a_1 N^k)(D_v^- f^k)_{i,1-j_{\max}} = 0, & \text{(C.3b)}
\end{cases}$$

Semi-implicit centered Euler method:

$$\begin{cases}
\textbf{Euler step:}\\
\dfrac{f_{i,j}^{k+1}-f_{i,j}^k}{\Delta t} + \mu_1^k D_x^c f_{i,j}^k + \mu_2^k D_v^c f_{i,j}^k - d_{i,j} f_{i,j}^k - (a_0+a_1 N^k)(D_v^2 f^{k+1})_{i,j} = N^k \rho_{i,j}, & \text{(C.4a)}\\
\textbf{Boundary Robin conditions:}\\
-(\mu_2^k)_{i,j_{\max}-1}^- f_{i,j_{\max}}^k - (a_0+a_1 N^k)(D_v^+ f^{k+1})_{i,j_{\max}-1} = 0,\\
(\mu_2^k)_{i,1-j_{\max}}^+ f_{i,-j_{\max}}^k - (a_0+a_1 N^k)(D_v^- f^{k+1})_{i,1-j_{\max}} = 0, & \text{(C.4b)}
\end{cases}$$

Fully explicit centered Euler method:

$$\begin{cases}
\textbf{Euler step:}\\
\dfrac{f_{i,j}^{k+1}-f_{i,j}^k}{\Delta t} + \mu_1^k D_x^c f_{i,j}^k + \mu_2^k D_v^c f_{i,j}^k - d_{i,j} f_{i,j}^k - (a_0+a_1 N^k)(D_v^2 f^k)_{i,j} = N^k \rho_{i,j}, & \text{(C.5a)}\\
\textbf{Boundary Robin conditions:}\\
-(\mu_2^k)_{i,j_{\max}-1}^- f_{i,j_{\max}}^k - (a_0+a_1 N^k)(D_v^+ f^k)_{i,j_{\max}-1} = 0,\\
(\mu_2^k)_{i,1-j_{\max}}^+ f_{i,-j_{\max}}^k - (a_0+a_1 N^k)(D_v^- f^k)_{i,1-j_{\max}} = 0, & \text{(C.5b)}
\end{cases}$$

Remark C.1. For the centered comparison schemes, the word "centered" refers only to the discretization of the transport terms inside the computational domain, meaning in $\mathcal{E}$. The artificial velocity boundaries are treated by the same one-sided Robin-type closure as in the main scheme. This choice is deliberately favorable to the centered schemes, since it preserves the same boundary-flux treatment across all algorithms.

Remark C.2. Similarly, the implementation uses the sign-split form of the vertical boundary drift. Under Assumption (2), this is equivalent to the unsplit formula, but it makes the intended orientation of the boundary flux explicit in the code.

D. Parameter values

Unless otherwise stated, $u_{\mathrm{R}} = 4$.

Table D.1
Parameters used for the accuracy and sensitivity tests of the mean-field approximation. Here $J = J_{\mathrm{E}}^{\mathrm{ext}} = J_{\mathrm{I}}^{\mathrm{ext}} = J_{\mathrm{E}}^{\mathrm{int}} = J_{\mathrm{I}}^{\mathrm{int}}$; a dash indicates that the corresponding parameter is not predetermined throughout the reference Table or Figure.

Parameter	Figs. 8 and 9	Table 5	Table 6	Table 7, Fig. 10	Table 8
Initial condition					
x_{init}	4	4	4	2	4
v_{init}	15	15	15	−15	15
σ_0	3	3	3	1	3
Phase-space domain					
$x_{\min}$	−9	−9	-	-	−21
$x_{\max}$	9	9	9	9	9
V	25	25	25	20	25
$\Delta x = \Delta v$	1/101	-	1/21	1/21	1/21
Physical constants					
$R = R_L$	0.8	0.8	0.8	0.8	0.8
C	1	1	1	1	1
L	2	2	2	2	2
τ_{syn}	2.5	2.5	2.5	2.5	2.5
Derived constants					
ω_0	1	1	1	1	1
τ	20/33	20/33	20/33	20/33	20/33
ν_{ext}	0.1	0.1	0.1	10	0.1
$b^{\mathrm{ext}} = b^{\mathrm{int}}$	6×10^{-3}	6×10^{-3}	-	-6×10^{-1}	6×10^{-3}
a_0	5×10^{-9}	5×10^{-9}	-	5×10^{-2}	5×10^{-9}
a_1	5×10^{-8}	5×10^{-8}	-	5×10^{-3}	5×10^{-8}
Connectivity					
$c_{\mathrm{E}}^{\mathrm{ext}} = c_{\mathrm{E}}^{\mathrm{int}}$	800	800	800	20	800
$c_{\mathrm{I}}^{\mathrm{ext}} = c_{\mathrm{I}}^{\mathrm{int}}$	200	200	200	80	200
J	2.5×10^{-5}	2.5×10^{-5}	-	2.5×10^{-2}	2.5×10^{-5}
Brian 2 population					
M_E	80000	80000	8000	2000	-
M_I	20000	20000	2000	8000	-
$M = M_E + M_I$	10^5	10^5	10^4	10^4	-
Number of Brian 2 runs					
Q	10	10	3	10	10
Time discretization					
T	1	1	1	10	1
Δt	10^{-5}	-	5×10^{-5}	10^{-3}	5×10^{-5}
Δt_{bin}	5×10^{-3}	5×10^{-3}	5×10^{-3}	5×10^{-3}	5×10^{-3}

In Table D.2, T denotes the final time used for the two-dimensional simulations and the corresponding time-series plots, as well as the 2D snapshots and 2D videos. The value T_{3D} is used only for the three-dimensional visualization of the density, while T_∞ denotes the final time used to compute the numerical long-time profile f^∞.

Table D.2
Experiment-dependent parameters used in the numerical exploratory tests.

Category	Parameter	Reset-driven regime	Subthreshold damped oscillations	Far from threshold	Feedback-driven oscillations
Initial condition					
	x_{init}	7	6	-10	$64/11$
	v_{init}	15	20	-5	0
	σ_0	1	1	2	0.8
Spatial domain					
	$x_{\min}$	-21	-31	-23	-21
	$x_{\max}$	9	9	9	9
	Δx	$1/19$	$1/21$	$1/15$	$1/11$
Velocity domain					
	$v_{\min}$	-30	-40	-30	-100
	$v_{\max}$	30	40	30	100
	Δv	$1/19$	$1/21$	$1/15$	$1/11$
Electrical constants					
	b	0.5	1	1	9
	ν_{ext}	1	10	1	0.6
	ω_0	0.01	0.5	1	1
	τ	100	5	1	500
	a_0	0.5	0.5	1	10^{-7}
	a_1	0.5	0.5	1	10^{-10}
Time step					
	Δt	4×10^{-5}	2×10^{-4}	1.6×10^{-4}	$13/28000$
Final times					
	T	0.4	10	8	130
	T_{3D}	0.4	20	8	195
	T_∞	20	50	40	650
Reset voltage value					
	u_{R}	4	4	4	$86/11$

Acknowledgements:

The author thanks Guillaume Dujardin (INRIA) and Pierre Roux (Ecole Centrale de Lyon) for many helpful remarks and ideas during the construction of this article, Francis Filbet (Université de Toulouse) for his expert feedback on numerical analysis, and Tatiana Engel (Stanford University) for her views on the neuronal model. Part of the work on numerical traces was carried out at Ecole Centrale de Lyon, which the author thanks for its hospitality. Nicolas Zadeh acknowledges support from the Fonds National de la Recherche Scientifique (FNRS) through travel grants used to visit Ecole Centrale de Lyon and attend ECMTB 2024.

References

[1] Adair, A., Owen-Newns, D., Donati, G., Robertson, J., Figueiredo, J., Wasige, E., Al-Taai, Q., Romeira, B., Hejda, M., Hurtado, A., 2026. Resonate-and-fire photonic-electronic spiking neurons for fast and efficient light-enabled neuromorphic processing systems. Commun. Phys. doi:10.1038/s42005-026-02694-5.

[2] Alasio, L., Bruna, M., Carrillo, J.A., 2020. The role of a strong confining potential in a nonlinear Fokker-Planck equation. Nonlinear Anal. 193, 111480. doi:10.1016/j.na.2019.03.003.
[3] Alonso, A., Llinás, R.R., 1989. Subthreshold Na+-dependent theta-like rhythmicity in stellate cells of entorhinal cortex layer II. Nature 342, 175–177. doi:10.1038/342175a0.
[4] Ambrogi, E., He, Q., Salort, D., 2026. Nonlinear stability for a two-dimensional fokker-planck equation with partial diffusion in neuroscience. Nonlinearity 39, 035013. doi:10.1088/1361-6544/ae4cec.
[5] Amit, D.J., Brunel, N., 1997. Model of global spontaneous activity and local structured activity during delay periods in the cerebral cortex. Cereb. Cortex 7, 237–252. doi:10.1093/cercor/7.3.237.
[6] Azam, M.A., Bhattacharya, D., Querlioz, D., Atulasimha, J., 2018. Resonate and fire neuron with fixed magnetic skyrmions. J. Appl. Phys. 124, 152122. doi:10.1063/1.5042308.
[7] Bartel, H., Lampert, J., Ranocha, H., 2024. Structure-preserving numerical methods for Fokker-Planck equations. PAMM 24. doi:10.1002/pamm.202400007.
[8] Blankenburg, S., Lindner, B., Schreiber, S., 2013. The information transmission in resonate-and-fire neuron models, in: Bernstein Conference 2013, Tübingen, Germany. doi:10.12751/nncn.bc2013.0209. Abstract T82, September 24–27, 2013.
[9] Blankenburg, S., Wu, W., Lindner, B., Schreiber, S., 2015. Information filtering in resonant neurons. J. Comput. Neurosci. 39, 349–370. doi:10.1007/s10827-015-0580-6.
[10] Brunel, N., 2000. Dynamics of sparsely connected networks of excitatory and inhibitory spiking neurons. J. Comput. Neurosci. 8, 183–208. doi:10.1023/a:1008925309027.
[11] Brunel, N., Hakim, V., 1999. Fast global oscillations in networks of integrate-and-fire neurons with low firing rates. Neural Comput. 11, 1621–1671. doi:10.1162/089976699300016179.
[12] Brunel, N., Wang, X.J., 2003. What determines the frequency of fast network oscillations with irregular neural discharges? I. synaptic dynamics and excitation-inhibition balance. J. Neurophysiol. 90, 415–430. doi:10.1152/jn.01095.2002.
[13] Cai, D., Tao, L., Rangan, A.V., McLaughlin, D.W., 2006. Kinetic theory for neuronal network dynamics. Commun. Math. Sci. 4, 97–127. doi:10.4310/CMS.2006.v4.n1.a4.
[14] Cai, D., Tao, L., Shelley, M., McLaughlin, D.W., 2004. An effective kinetic representation of fluctuation-driven neuronal networks with application to simple and complex cells in visual cortex. Proc. Natl. Acad. Sci. U.S.A. 101, 7757–7762. doi:10.1073/pnas.0401906101.
[15] Carrillo, J., Perthame, B., Salort, D., Smets, D., 2015. Qualitative properties of solutions for the noisy integrate & fire model in computational neuroscience. Nonlinearity 28, 3365. doi:10.1088/0951-7715/28/9/3365.
[16] Carrillo, J.A., González, M.d.M., Gualdani, M.P., Schonbek, M.E., 2013. Classical solutions for a nonlinear Fokker-Planck equation arising in computational neuroscience. Commun. Partial Differ. Equ. 38, 385–409. doi:10.1080/03605302.2012.747536.
[17] Carrillo, J.A., Roux, P., 2025. Nonlinear partial differential equations in neuroscience: From modeling to mathematical theory. Mathematical Models and Methods in Applied Sciences 35, 403–584. doi:10.1142/S0218202525400044.
[18] Chang, J.S., Cooper, G., 1970. A practical difference scheme for Fokker-Planck equations. J. Comput. Phys. 6, 1–16. doi:10.1016/0021-9991(70)90001-X.
[19] Chartrand, T., Goldman, M.S., Lewis, T.J., 2019. Synchronization of electrically coupled resonate-and-fire neurons. SIAM J. Appl. Dyn. Syst. 18, 1643–1693. doi:10.1137/18M1197412.
[20] Cáceres, M., Roux, P., Salort, D., Schneider, R., 2019. Global-in-time solutions and qualitative properties for the NNLIF neuron model with synaptic delay. Commun. Partial Differ. Equ. 44, 1358–1386. doi:10.1080/03605302.2019.1639732.
[21] Cáceres, M.J., Carrillo, J.A., Perthame, B., 2011. Analysis of nonlinear noisy integrate & fire neuron models: blow-up and steady states. J. Math. Neurosci. 1, 7. doi:10.1186/2190-8567-1-7.
[22] Cáceres, M.J., Cañizo, J.A., Ramos-Lora, A., 2024. The sequence of pseudo-equilibria describes the long-time behaviour of the NNLIF model with large delay. Phys. Rev. E 110, 064308. doi:10.1103/PhysRevE.110.064308.
[23] Cáceres, M.J., Cañizo, J.A., Ramos-Lora, A., 2025. On the asymptotic behavior of the NNLIF neuron model for general connectivity strength. Commun. Math. Phys. 406. doi:10.1007/s00220-025-05287-5.
[24] Cáceres, M.J., Schneider, R., 2018. Analysis and numerical solver for excitatory-inhibitory networks with delay and refractory periods. ESAIM Math. Model. Numer. Anal. 52, 1733–1761. doi:10.1051/m2an/2018014.
[25] Delarue, F., Inglis, J., Rubenthaler, S., Tanré, E., 2013. First hitting times for general non-homogeneous 1d diffusion processes: density estimates in small time. HAL: hal-00870991.
[26] Delarue, F., Inglis, J., Rubenthaler, S., Tanré, E., 2015. Particle systems with a singular mean-field self-excitation. application to neuronal networks. Stoch. Process. Appl. 125, 2451–2492. doi:10.1016/j.spa.2015.01.007.
[27] Dou, X., Perthame, B., Salort, D., Zhou, Z., 2023. Bounds and long term convergence for the voltage-conductance kinetic system arising in neuroscience. Discrete and Continuous Dynamical Systems 43, 1366–1382. doi:10.3934/dcds.2022136.
[28] Dou, X., Zhou, Z., 2025. Dilating blow-up time: A generalized solution of the NNLIF neuron model and its global well-posedness. Commun. Math. Sci. 23, 1081–1138. doi:10.4310/CMS.250412104353.
[29] Dujardin, G., Hérau, F., Lafitte, P., 2020. Coercivity, hypocoercivity, exponential time decay and simulations for discrete Fokker-Planck equations. Numer. Math. 144, 615–697. doi:10.1007/s00211-019-01094-y.
[30] Engel, T.A., Schimansky-Geier, L., Herz, A., Schreiber, S., Erchova, I., 2008. Subthreshold membrane-potential resonances shape spike-train patterns in the entorhinal cortex. J. Neurophysiol. 100, 1576–1589. doi:10.1152/jn.01282.2007.
[31] Erchova, I., Kreck, G., Heinemann, U., Herz, A.V.M., 2004. Dynamics of rat entorhinal cortex layer II and III cells: characteristics of membrane potential resonance at rest predict oscillation properties near threshold. J. Physiol. 560, 89–110. doi:10.1113/jphysiol.2004.069930.
[32] Filbet, F., Yang, C., 2013. An inverse Lax-Wendroff method for boundary conditions applied to Boltzmann type models. J. Comput. Phys. 245, 43–61. doi:10.1016/j.jcp.2013.03.015.

[33] FitzHugh, R., 1955. Mathematical models of threshold phenomena in the nerve membrane. Bull. Math. Biophys. 17, 257–278. doi:10.1007/BF02477753.
[34] Fonte Sánchez, C., Mischler, S., Salort, D., 2026. Existence of solutions to the voltage-conductance kinetic equation in a general conductivity regime. arXiv:2607.22112.
[35] Fonte Sánchez, C., Mischler, S., 2024. On the voltage-conductance kinetic equation. arXiv:2408.02471.
[36] Gutfreund, Y., Yarom, Y., Segev, I., 1995. Subthreshold oscillations and resonant frequency in guinea-pig cortical neurons: physiology and modelling. J. Physiol. 483, 621–640. doi:10.1113/jphysiol.1995.sp020611.
[37] Herda, M., Monmarché, P., Perthame, B., 2025. Wasserstein contraction for the stochastic Morris-Lecar neuron model. Kinet. Relat. Models 18, 1–18. doi:10.3934/krm.2024009.
[38] Higuchi, S., Kairat, S., Bohte, S., Otte, S., 2024. Balanced resonate-and-fire neurons, in: Proceedings of the 41st International Conference on Machine Learning, PMLR. pp. 18305–18323.
[39] Hodgkin, A.L., Huxley, A.F., 1952. A quantitative description of membrane current and its application to conduction and excitation in nerve. J. Physiol. 117, 500–544. doi:10.1113/jphysiol.1952.sp004764.
[40] Hu, J., Liu, J.G., Xie, Y., Zhou, Z., 2021. A structure preserving numerical scheme for Fokker-Planck equations of neuron networks: Numerical analysis and exploration. J. Comput. Phys. 433, 110195. doi:10.1016/j.jcp.2021.110195.
[41] Huber, T.E., Lecomte, J., Polovnikov, B., von Arnim, A., 2025. Scaling up resonate-and-fire networks for fast deep learning, in: Computer Vision – ECCV 2024 Workshops. Springer Nature Switzerland, Cham. volume 15059 of *Lecture Notes in Comput. Sci.*, pp. 241–258. doi:10.1007/978-3-031-92460-6_15.
[42] Hörmander, L., 1967. Hypoelliptic second order differential equations. Acta Math. 119, 147–171. doi:10.1007/BF02392081.
[43] Ikeda, K., Roux, P., Salort, D., Smets, D., 2022. Theoretical study of the emergence of periodic solutions for the inhibitory NNLIF neuron model with synaptic delay. Math. Neurosci. Appl. 2. doi:10.46298/mna.7256.
[44] Izhikevich, E., 2004. Which model to use for cortical spiking neurons? IEEE Trans. Neural Netw. 15, 1063–1070. doi:10.1109/TNN.2004.832719.
[45] Izhikevich, E.M., 2001. Resonate-and-fire neurons. Neural Netw. 14, 883–894. doi:10.1016/S0893-6080(01)00078-8.
[46] Jin, S., 2022. Asymptotic-preserving schemes for multiscale physical problems. Acta Numer. 31, 415–489. doi:10.1017/S0962492922000010.
[47] Jin, S., Yan, B., 2011. A class of asymptotic-preserving schemes for the Fokker-Planck-Landau equation. J. Comput. Phys. 230, 6420–6437. doi:10.1016/j.jcp.2011.04.002.
[48] Krupa, M., Touboul, J.D., 2016. Complex oscillations in the delayed FitzHugh-Nagumo equation. J. Nonlinear Sci. 26, 43–81. doi:10.1007/s00332-015-9268-3.
[49] Lapicque, L., 1907. Recherches quantitatives sur l'excitation électrique des nerfs traitée comme une polarisation. J. Physiol. Pathol. Gen. 9, 620–635.
[50] Mauro, A., Conti, F., Dodge, F., Schor, R., 1970. Subthreshold behavior and phenomenological impedance of the squid giant axon. J. Gen. Physiol. 55, 497–523. doi:10.1085/jgp.55.4.497.
[51] Mischler, S., Quiñinao, C., Touboul, J., 2016. On a kinetic FitzHugh-Nagumo model of neuronal network. Commun. Math. Phys. 342, 1001–1042. doi:10.1007/s00220-015-2556-9.
[52] Morris, C., Lecar, H., 1981. Voltage oscillations in the barnacle giant muscle fiber. Biophys. J. 35, 193–213. doi:10.1016/S0006-3495(81)84782-0.
[53] Paekivi, S., Mankin, R., Rekker, A., 2017. Memory effects on a resonate-and-fire neuron model subjected to Ornstein-Uhlenbeck noise, in: AIP Conference Proceedings. doi:10.1063/1.5007393.
[54] Perthame, B., Salort, D., 2013. On a voltage-conductance kinetic system for integrate & fire neural networks. Kinet. Relat. Models 6, 841–864. doi:10.3934/krm.2013.6.841.
[55] Protachevicz, P.R., Bonin, C.A., Iarosz, K.C., Caldas, I.L., Batista, A.M., 2022. Large coefficient of variation of inter-spike intervals induced by noise current in the resonate-and-fire model neuron. Cogn. Neurodyn. doi:10.1007/s11571-022-09789-z.
[56] Renart, A., Brunel, N., Wang, X.J., 2003. Mean-field theory of irregularly spiking neuronal populations and working memory in recurrent cortical networks, Chapman and Hall/CRC Press. doi:10.1201/9780203494462.ch15.
[57] Ricciardi, L.M., 1977. Diffusion Processes and Related Topics in Biology. Springer Berlin Heidelberg. doi:10.1007/978-3-642-93059-1.
[58] Rieutord, C., Salort, D., 2026. Asymptotic dynamics of inhibitory networks for the nnlif model in the large-delay limit arXiv:2606.17611.
[59] Risken, H., 1996. The Fokker-Planck Equation. Springer Berlin, Heidelberg. doi:10.1007/978-3-642-61544-3.
[60] Rowland, D.C., Obenhaus, H.A., Skytøen, E.R., Zhang, Q., Kentros, C.G., Moser, E.I., Moser, M.B., 2018. Functional properties of stellate cells in medial entorhinal cortex layer II. eLife 7, e36664. doi:10.7554/eLife.36664.
[61] Salort, D., Smets, D., 2024. Convergence towards equilibrium for a model with partial diffusion. Communications in Partial Differential Equations 49, 410–427. doi:10.1080/03605302.2024.2344806.
[62] Stimberg, M., Brette, R., Goodman, D.F., 2019. Brian 2, an intuitive and efficient neural simulator. eLife 8, e47314. doi:10.7554/eLife.47314.
[63] Ukai, S., 1986. Solutions of the boltzmann equation, in: Studies in Mathematics and Its Applications. volume 18, pp. 37–96. doi:10.1016/S0168-2024(08)70128-0.
[64] V-Ghaffari, B., Kouhnavard, M., Elbasiouny, S.M., 2017. Mixed-mode oscillations in pyramidal neurons under antiepileptic drug conditions. PLOS ONE 12, e0178244. doi:10.1371/journal.pone.0178244.
[65] Verechtchaguina, T., Sokolov, I., Schimansky-Geier, L., 2007. Interspike interval densities of resonate and fire neurons. Biosystems 89, 63–68. doi:10.1016/j.biosystems.2006.03.014.
[66] Verechtchaguina, T., Sokolov, I.M., Schimansky-Geier, L., 2006. First passage time densities in resonate-and-fire models. Phys. Rev. E 73, 031108. doi:10.1103/PhysRevE.73.031108.

[67] Villacorta, J.A., Panetsos, F., 2005. Information coding by ensembles of resonant neurons. Biol. Cybern. 92, 339–347. doi:10.1007/s00422-005-0554-2.

[68] White, J.A., Rubinstein, J.T., Kay, A.R., 2000. Channel noise in neurons. Trends Neurosci. 23, 131–137. doi:10.1016/S0166-2236(99)01521-0.

[69] Zadeh, N., 2026a. Finite-difference scheme for a nonlinear kinetic Fokker-Planck equation arising from noisy resonate and fire neuronal networks. Zenodo. doi:10.5281/zenodo.21246913. version v1.0.0.

[70] Zadeh, N., 2026b. Kinetic description and numerical study of a network of noisy resonate and fire neurons - long version. Cambridge Open Engage. doi:10.33774/coe-2026-n2ssp. preprint.

[71] Zhang, D., Zhang, M., Wang, S., Wang, J., Wei, W., Ma, Z., Wang, G., Yang, Y., Li, H., 2025. Dendritic resonate-and-fire neuron for effective and efficient long sequence modeling. arXiv:2509.17186.